Monthly Notices
of the
ROYAL ASTRONOMICAL SOCIETY

MNRAS **491,** 2688–2705 (2020)
Advance Access publication 2019 November 15

doi:10.1093/mnras/stz3160

Estimating trajectories of meteors: an observational Monte Carlo approach – I. Theory

Denis Vida [1,2★] Peter S. Gural,[3★] Peter G. Brown,[2,4★] Margaret Campbell-Brown [2,4] and Paul Wiegert[2,4]

[1]*Department of Earth Sciences, University of Western Ontario, London, Ontario N6A 5B7, Canada*
[2]*Department of Physics and Astronomy, University of Western Ontario, London, Ontario N6A 3K7, Canada*
[3]*Gural Software and Analysis LLC, Sterling, VA 20164, USA*
[4]*Centre for Planetary Science and Exploration, University of Western Ontario, London, Ontario N6A 5B8, Canada*

Accepted 2019 November 7. Received 2019 October 28; in original form 2019 March 31

ABSTRACT

It has recently been shown by Egal et al. that some types of existing meteor in-atmosphere trajectory estimation methods may be less accurate than others, particularly when applied to high-precision optical measurements. The comparative performance of trajectory solution methods has previously only been examined for a small number of cases. Besides the radiant, orbital accuracy depends on the estimation of pre-atmosphere velocities, which have both random and systematic biases. Thus, it is critical to understand the uncertainty in velocity measurement inherent to each trajectory estimation method. In this first of a series of two papers, we introduce a novel meteor trajectory estimation method that uses the observed dynamics of meteors across stations as a global optimization function and that does not require either a theoretical or an empirical flight model to solve for velocity. We also develop a 3D observational meteor trajectory simulator that uses a meteor ablation model to replicate the dynamics of meteoroid flight, as a means to validate different trajectory solvers. We both test this new method and compare it to other methods, using synthetic meteors from three major showers spanning a wide range of velocities and geometries (Draconids, Geminids, and Perseids). We determine which meteor trajectory solving algorithm performs better for all-sky, moderate field-of-view, and high-precision narrow-field optical meteor detection systems. The results are presented in the second paper in this series. Finally, we give detailed equations for estimating meteor trajectories and analytically computing meteoroid orbits, and provide the PYTHON code of the methodology as open-source software.

Key words: comets – meteors – meteoroids; methods: data analysis.

1 INTRODUCTION

Schiaparelli & von Boguslawski (1871) were the first to show the connection between the orbits of meteor showers and comets (Romig 1966; Hughes 1982). This physical connection motivated development of various methods of estimating meteor trajectories, with the first reasonably precise measurements made even earlier with the pioneering work of Brandes and Benzenberg in the late 18th century (Burke 1986). These techniques typically use optical measurements from multiple sites to estimate atmospheric meteor trajectories. Gural (2012) provides a good historical overview.

In this work, we focus on three foundational papers that provide representative descriptions of the three most common modern meteor trajectory estimation methods:

(i) the intersecting planes (IP) method as described by Ceplecha (1987);
(ii) the line-of-sight (LoS) method by Borovička (1990);
(iii) the multiparameter fit (MPF) method of Gural (2012).

The goal of any trajectory solver is to reconstruct the atmospheric trajectory of a meteor, leading ultimately to an estimate of its pre-atmospheric orbit. The trajectory is defined by a position vector (a reference position in space) and a velocity vector. To compute a reliable heliocentric orbit, this should preferably be at a point before any significant deceleration of the meteoroid occurs. A common assumption is that the trajectory is a straight line, a good approximation for shorter meteors. However, longer meteors, particularly those entering at shallow angles, may show significant deviation from a straight-line trajectory due to Earth's gravity (Ceplecha 1979).

Existing methods usually estimate the geometry of the meteor path separately from the dynamics of the meteoroid (i.e. the time-

★ E-mail: dvida@uwo.ca (DV); pgural@gmail.com (PSG); pbrown@uwo.ca (PGB)

dependent characteristics of the meteor: position, velocity, and acceleration). The velocity can be estimated by fitting an empirical model to the observations of time versus path-length from the beginning of the meteor. Gural (2012) was the first to note that trajectories can be better constrained by fitting a meteor propagation model to both the meteor trajectory geometry and the meteoroid dynamics at the same time. This assumption makes use of the fact that all observers should see the same dynamical behaviour of a particular meteoroid at the same point in time. A consequence of this approach is that it allows an estimate of the absolute timing offsets between stations. A further recent advance in this area is using particle filters to directly fit numerical meteor ablation models to better estimate trajectories of fireballs (Sansom, Rutten & Bland 2017).

The original motivation for this work was earlier analysis of two-station meteor data obtained by the Canadian Automated Meteor Observatory (CAMO) mirror tracking system (Weryk et al. 2013). The system achieves an angular precision for meteor positions of the order of a few arcseconds (limited largely by the system's ability to resolve the physical spreading of the meteor itself; Stokan et al. 2013), which translates to a spatial precision of a few metres. The temporal precision of the system is 10 ms. This is sufficient to discern individual fragments of fragmenting faint meteors (Subasinghe, Campbell-Brown & Stokan 2016; Vida et al. 2018a). Similar to Egal et al. (2017), we found that the existing methods of trajectory estimation do not always provide solutions of satisfactory quality. For example, we often found with CAMO measurements that the IP and the LoS method produce solutions where the dynamics of the meteor do not match at different stations. The MPF method, in some cases, depending on the velocity model used, had convergence issues. This suggested that in some cases forcing the meteoroid velocity to follow a closed-form empirical model did not result in a physically consistent solution. As a result of this experience, we also wanted to objectively quantify the real uncertainties and formally define the true accuracy of individually measured meteor radiants and velocities as estimated using CAMO data, and by extension other optical systems.

This series of papers attempts to answer the following question: For a given type of optical system, what is the best trajectory solver to use, and what quantitative accuracy should one typically expect? We note that this is one step in the process of defining the best estimate for a meteoroid's original heliocentric orbit. The necessary additional step is accounting for deceleration due to atmospheric drag on the earliest measured luminous point of the meteor, a topic addressed in an earlier paper (Vida, Brown & Campbell-Brown 2018b).

In the following sections, we discuss in detail the theory behind various methods of trajectory estimation and describe our novel Monte Carlo approach. Finally, for completeness, we summarize the equations for analytically computing meteoroid orbits from trajectory information, as previously published procedures were ambiguous in several crucial steps.

2 OVERVIEW OF TRAJECTORY SOLVERS

A set of LoS (angle–angle) measurements of meteor positions from an individual observing station describes a fan of rays when converted into a station-fixed Cartesian coordinate system. By assuming that the position of an observer can be represented by a single point in the same coordinate system (usually at the time of the middle of the meteor's trajectory), a plane can be fit through these points (Ceplecha 1987). By repeating the procedure for N different stations, one plane for each station is obtained. The intersection of every pair of planes, $\binom{N}{2}$ pairs in total, results in a line that describes the optimal trajectory as measured from two stations. If there are more than two trajectory lines, the average of the trajectories can be computed weighted by the squared sine of the convergence angle between every plane pair. The convergence angle is the angle between a pair of planes.

Borovička (1990) points out a disadvantage of the IP method: when the planes are paired using observations from multiple stations, the information about the uncertainty of individual measurements can be lost because only the whole plane is taken into consideration when intersecting it with another to define a trajectory. An outlier LoS measurement can shift the whole plane in a certain direction and influence the resulting trajectory. However, the fit residuals will not show the influence from the sole outlier.

Instead of pairing planes from individual stations and producing the trajectory as a secondary product, Borovička (1990) proposes that one can consider every measurement of meteor position as a ray emanating from the observer in the direction of the meteor at a specific point along its linear track. Each ray is usually referred to as an LoS measurement of the meteor. The trajectory is then found as the 3D line that results in the minimal distance to all measurement lines of sight, with the solution computed using a least-squares minimization. Furthermore, Borovička (1990) points out that this method can compensate for Earth's rotation at each LoS observation directly during the trajectory estimation process. In the absence of this compensation, fixed observers on the non-inertial rotating surface of the Earth perceive a virtual force (the Coriolis force) on the apparent meteor trajectory.

Additionally, the Borovička (1990) method makes possible compensation for diurnal aberration, an effect due to the Earth's rotation that occurs because of the changing observer's perspective of the meteor with respect to distant stars. Assuming one knows the absolute time, an Earth-centred inertial (ECI) reference frame can be adopted in which the observer's coordinates are constantly changing due to Earth's rotation, but the meteor trajectory remains linear. We use the definition of ECI coordinates where the X-axis is aligned with the mean equinox at 12:00 Terrestrial Time on 2000 January 1 (J2000).

In the original LoS paper, Borovička (1990) keeps the observers in the Earth-centred Earth-fixed frame (ECEF), presumably because the timing of each individual measurement (taken on a single photographic film in that era) was unknown. In contrast to the ECI system, which does not rotate with respect to the stars but the coordinates of observers on Earth's surface are changing in time, coordinates of ECEF are fixed with respect to the Earth's surface. Without correcting for the changes in observer positions, Borovička (1990) found the results of the IP and LoS methods comparable. The reason that it is not possible to account for moving observers in the IP method is that the motion of the observer and the positions of the meteor are not coplanar (unless all measurements coincide with the observer's zenith, an impossible geometry to have from two different stations).

To provide a concrete estimate of the magnitude of the diurnal aberration correction, let us consider an observer at a latitude of 45°N where the Earth's rotational east–west velocity is about 328 m s^{-1}. For a meteor of 1 s duration, the real position of the observer will change $\pm$164 m with respect to the average time of the trajectory determination. There is also a small effect when two observers are not at equal latitudes. A second observer at 46°N ($\sim$120 km away) experiences a rotational velocity of

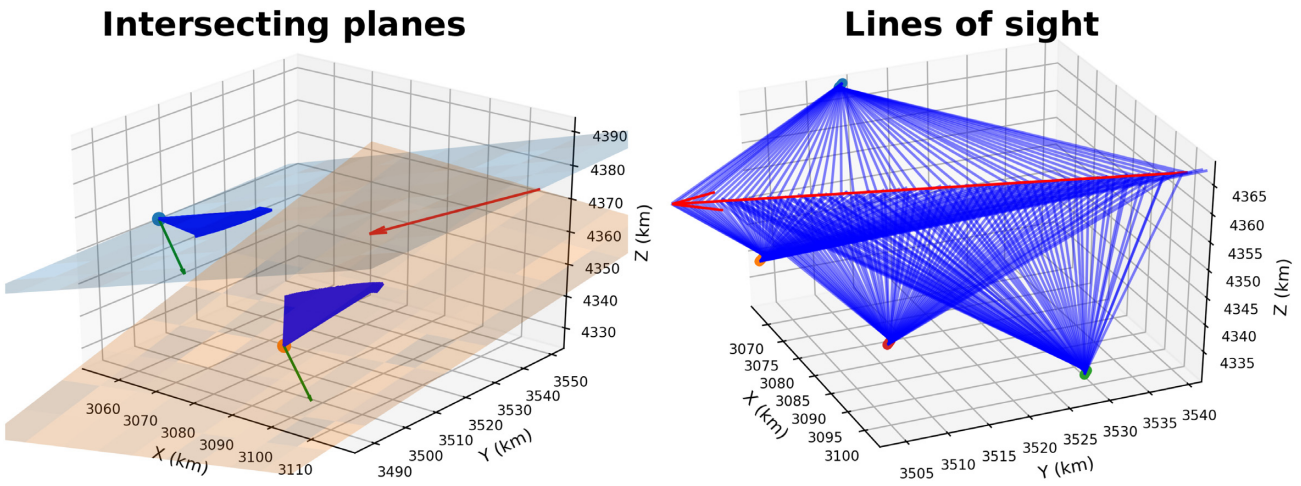

Figure 1. *Left:* The IP method with only the two stations having the best convergence angle shown. The planes are shown in blue and orange (semitransparent) and are coplanar with LoS observations (blue arrows emanating from stations). Note that stations are single points in the ECEF frame, but here we show them in the ECI frame at a fixed time. The green arrows are plane normals from each station, and the red arrow is the resulting estimated trajectory. *Right:* The LoS method, where coordinates of all four stations are changing due to the Earth's rotation.

322 m s^{-1}, which causes a differential of 3 m between the first and the last positions of the two observers. This effect is minor if positional errors are orders of magnitude larger, but it has to be taken into account when estimating high-precision trajectories where positional measurements are of the order of metres. Fig. 1 shows a general comparison between the IP and the LoS method.

The MFP method was first presented at the 2011 International Meteor Conference with the underlying algorithmic details described in Gural (2012). It had been developed for the CAMS project, where the full processing pipeline is described in Jenniskens et al. (2011). In contrast to the IP and LoS methods, which are purely geometrical, the MPF method uses a velocity model (i.e. dynamical information) as well. By assuming an empirical velocity model that may include deceleration terms, the MPF method finds a trajectory solution (a line in 3D space) as well as the velocity and deceleration coefficients that best describe the observed meteor's observations from all stations given the constraints of the empirical dynamical model. Because of the dynamical constraints, the method is also able to estimate relative timing offsets between camera sites.

To avoid issues of confusion with local minima in the method's cost function, an initial guess for the solution is obtained using the IP method. This guess is further refined using the LoS method – the latter is modified by minimizing the angles between the measured lines of sight and the model trajectory, instead of minimizing the distances between the two. This refined guess is fed into a simplex-based non-linear equation solver where the angles between the measured lines of sight and the positions predicted by the model are minimized. This effectively ensures that all observers 'see' the same dynamics of the meteor in time.

Because observing systems usually do not have absolute synchronized time, the time difference between the observers must be estimated as well in the MPF. In Gural (2012), the MPF method was compared to the IP and LoS methods using data from wide-field systems. The results showed that the radiant dispersion of meteor showers is significantly smaller if the MPF method with a constant velocity model (i.e. no deceleration) is used, especially for cases with small convergence angles. The authors proposed three meteor propagation models:

(i) The constant velocity model:

$$d(t) = v_0 t, \tag{1}$$

where $d(t)$ is the distance of the meteor at a particular point in time after the beginning point and v_0 is the constant velocity of the meteor.

(ii) The linear deceleration model:

$$d(t) = \begin{cases} v_0 t, & \text{if } t < t_0, \\ v_0 t - \frac{1}{2} a (t - t_0)^2, & \text{otherwise}, \end{cases} \tag{2}$$

where t_0 is the time when meteor begins decelerating with a constant deceleration a.

(iii) The empirical exponential deceleration model of Whipple & Jacchia (1957):

$$d(t) = v_0 t - |a_1| e^{|a_2| t}, \tag{3}$$

where a_1 and a_2 are deceleration parameters.

The complexities due to the physical properties of the meteoroids and their resulting ablation behaviour are not included in these models. The exponential deceleration model is the only one motivated by a physical basis, namely, that the meteoroid's deceleration is proportional to the atmospheric density, following classical single-body ablation models (Ceplecha et al. 1998). As the atmospheric density increases exponentially with decreasing height, the velocity should follow a similar functional trend. However, the single-body assumption breaks down when a meteoroid starts fragmenting, a behaviour shown to exist for at least 90 per cent of meteors from high-precision observations (Subasinghe et al. 2016), a phenomenon understood to be ubiquitous across all meteoroid masses (Hawkes & Jones 1975; Ceplecha et al. 1998). Comparing the performance of different trajectory estimation methods even for single-body ablation has not been rigorously addressed. Gural (2012) performed simulations for a constant velocity model over an extensive range of encounter geometries and speeds. However, the comparison did not examine other functional forms of deceleration.

In recent work by Egal et al. (2017), it was shown that the exponential model is difficult to fit using local cost function

minimization methods since it is mathematically ill-conditioned and the associated model coefficients have linear dependence. The authors showed the advantages of global minimization methods over local techniques. In particular, they applied the particle swarm optimization (PSO) method (Eberhart & Kennedy 1995) for fitting the exponential deceleration model and showed that it produced superior results, albeit at the expense of higher computational costs. Their work has shown that the fit works well on simulated data produced using the exponential deceleration model. In contrast, the fits were poorer when model data were created using the meteor ablation model of Borovička, Spurnỳ & Koten (2007). They concluded that of all methods tested (IP, LoS, and MPF), the MPF method consistently produced results with the smallest residuals and good radiant solutions even for meteors with very low convergence angles ($Q_c \sim 1^\circ$). They also showed that the initial velocity estimated from all of the trajectory solvers for ablation-simulated meteoroids was not accurately determined. This suggests that a more reliable meteor propagation model is needed for the MPF in particular.

We have directly used all implementations of the three trajectory solvers including the PSO-based implementation of the Gural (2012) method, to test their relative performance on high-precision CAMO data. Given the performance limitations of existing algorithms, it was decided to develop a Monte Carlo trajectory solver specifically to attempt to improve the accuracy of meteor trajectory solutions where high-precision data are available. The details of this trajectory solver are given in Section 3. To verify the performance of this new method and compare to the three other solvers, we also developed an observational meteor trajectory simulator. This provides synthetic measurement inputs to each solver using known solutions; details are given in Section 4.

We emphasize that the ultimate limitation to the accuracy in the estimation of a meteoroid orbit based on observations of a meteor in the atmosphere is the amount of deceleration that occurs prior to the luminous phase. We use the term 'initial velocity' for the velocity of the meteor at the moment of first detection and 'pre-atmospheric velocity' for the velocity before any significant deceleration has occurred (we assume this to be at a height of 180 km). The difference between the initial velocity and the pre-atmospheric velocity for various types of meteoroids as measured by several typical observation systems was analysed in Vida et al. (2018b). It was found that low-velocity meteors significantly decelerate [up to 750 m s^{-1} for moderate and narrow field-of-view (FOV) optical systems] prior to sensor detection of the visible meteor trail. The proposed correction of Vida et al. (2018b) should be used to reconstruct the real pre-atmosphere velocity from the measured initial velocity. Establishing the latter quantity and its true uncertainty is the focus of this work.

3 MONTE CARLO TRAJECTORY ESTIMATION METHOD

Our newly developed method of trajectory estimation builds on the work of Gural (2012) and expands on an earlier similar approach described in Weryk & Brown (2012). This technique uses the IP and the LoS method to obtain a first estimate of the trajectory solution, and then uses the observed angular residuals between the measurements and the fitted trajectory as a direct estimate of the uncertainty. With these estimates in hand, Monte Carlo runs are then generated by adding Gaussian noise to the observations using the standard deviation of the angular residuals from the initial trajectory estimate and redoing the trajectory solution using noise-added data.

This procedure gives a set of trajectories that are geometrically possible to fit within the measurement uncertainty. The lines of sight from individual stations are then projected to the trajectory line and the dynamics of the meteor as seen from every station are computed. Critically in this new technique, the best solution is chosen by comparing the observed dynamics between different stations and choosing the trajectory that has the most consistent dynamics as seen from all stations. This approach constrains the trajectory solution both geometrically and dynamically without limiting the motion to an empirical propagation/ablation model, while simultaneously keeping LoS vectors within measurement uncertainty. Note that unlike in the MPF method, the geometry and dynamics are solved separately; the dynamics is only used as an additional constraint on the geometry.

Here, we provide detailed formulations of all the equations used by this trajectory solver, with the exception of well-known mathematical and numerical methods. The equations are given in a way that would make their computer implementation unambiguous and thus may slightly deviate from standard mathematical notation. Where the function for the four-quadrant inverse tangent is used, we assume that the order of arguments is atan2(y, x), as in C, FORTRAN, PYTHON, and MATLAB. This differs from MATHEMATICA and MS EXCEL whose implementations have the two arguments reversed. mod is the modulo operator, the integer division remainder operation. The PYTHON implementation of both the simulator and the solver is open source and publicly available at https://github.com/wmpg/WesternMeteorPyLib.

3.1 Inputs and conversions to rectangular coordinates

For every station $k \in \{1, \ldots, N_{\text{stations}}\}$, we have measurements $j \in \{1, \ldots, N_{\text{meas}(k)}\}$, producing inputs to the trajectory solver:

(i) Relative time t_{kj} in seconds of each measurement from every station, relative to the reference Julian date JD_{ref}.

(ii) Angular measurements of meteor positions in the horizontal coordinate system: azimuth measured eastward from the north A_{kj}, and altitude above the horizon a_{kj} for the epoch of date from each station. Equivalently, right ascension α and declination δ may be used, which can be converted to azimuth and altitude using equations given in Appendix G. If the equatorial coordinates are given in the J2000 epoch, care must be taken to first precess them to the epoch of date (see Appendix H). The epoch of date is assumed to be at JD_{ref}.

(iii) Geographical coordinates of every station: geodetic latitude φ_k, longitude λ_k, and height above a WGS84 Earth ellipsoid h_k [note that this height is not the same as the mean sea level (MSL) height reported by Google Earth and newer GPS devices – the difference can be up to 100 m].

The first step in the process is to compute the Julian date of every individual measurement:

$$\text{JD}_{kj} = \text{JD}_{\text{ref}} + t_{kj}/86\,400. \quad (4)$$

These times get updated in the second stage of the iteration when the trajectory is recomputed after the timing offset estimation. Next, measurements are converted to equatorial coordinates for the epoch of date using equations given in Appendix F. Two sets of equatorial coordinates are obtained: the first assumes the stations are fixed at JD_{ref} and is used for the IP method, while the second one takes into account the movement of the stations at each measurement time-step. Thus, when computing values for the IP method, the JD_{ref} reference time should be used for all measurement points. When computing values for the LoS method, the Julian date JD_{kj} of the individual measurements should be used. The measurements are

then converted to Cartesian unit vectors using equation (5). These vectors define the direction of the line of sight from a given station at each measurement point in time.

$$\xi = \cos\delta\cos\alpha,$$

$$\eta = \cos\delta\sin\alpha,$$

$$\zeta = \sin\delta. \tag{5}$$

The geographical positions of the stations are converted to ECI coordinates relative to the centre of the Earth using equations given in Appendix D1. Two sets of coordinates are calculated: X_{kj}, Y_{kj}, Z_{kj} for the position of each station at every point in time JD_{kj} and X'_k, Y'_k, Z'_k for stations fixed at JD_{ref}. ECI coordinates fixed at JD_{ref} are needed for the IP method, as this method implicitly assumes that the station is a point and its coordinates cannot move in time.

3.2 Plane fits

The best-fitting plane for observations from one station can be defined as

$$a\boldsymbol{x} + b\boldsymbol{y} + d = -\boldsymbol{z}, \tag{6}$$

where $\boldsymbol{x}$, $\boldsymbol{y}$, $\boldsymbol{z}$ are data vectors containing Cartesian unit vectors of directions ξ, η, ζ, and a zero, which represents the position of the station, taken to be the origin of the direction vector's coordinate system:

$$\boldsymbol{x} = [0, \xi_{k1}, \ldots, \xi_{kN_{\mathrm{meas}(k)}}],$$

$$\boldsymbol{y} = [0, \eta_{k1}, \ldots, \eta_{kN_{\mathrm{meas}(k)}}],$$

$$\boldsymbol{z} = [0, \zeta_{k1}, \ldots, \zeta_{kN_{\mathrm{meas}(k)}}]. \tag{7}$$

The problem can be written in data matrix form as

$$\begin{bmatrix} x_1 & y_1 & 1 \\ x_2 & y_2 & 1 \\ & \vdots & \\ x_n & y_n & 1 \end{bmatrix} \begin{bmatrix} a \\ b \\ d \end{bmatrix} = - \begin{bmatrix} z_1 \\ z_2 \\ \vdots \\ z_n \end{bmatrix}. \tag{8}$$

If we take the data matrix and pre-multiply both sides of the equation by its transpose, and invert to solve for the unknowns, we perform the equivalent of a linear least-squares fit. One should normalize the points to be relative to their mean, $\bar{x}$, $\bar{y}$, $\bar{z}$, in which case d can be excluded and one dimension can be dropped. Thus, the matrix equation solution can be written as

$$\begin{bmatrix} a \\ b \end{bmatrix} = - \begin{bmatrix} \sum_{i=1}^{n}(x_i - \bar{x})^2 & \sum_{i=1}^{n}(x_i - \bar{x})(y_i - \bar{y}) \\ \sum_{i=1}^{n}(x_i - \bar{x})(y_i - \bar{y}) & \sum_{i=1}^{n}(y_i - \bar{y})^2 \end{bmatrix}^{-1} \times \begin{bmatrix} \sum_{i=1}^{n}(x_i - \bar{x})(z_i - \bar{z}) \\ \sum_{i=1}^{n}(y_i - \bar{y})(z_i - \bar{z}) \end{bmatrix}. \tag{9}$$

After solving the matrix, the direction normal to the fit plane is

$$\boldsymbol{n} = [a, b, 1]^{\mathrm{T}}. \tag{10}$$

3.3 Plane intersections

We now consider planes in point-normal form. After finding the unit plane normal $\hat{\boldsymbol{n}}_k$ for observations from every station, we make use of the additional constraint that each normal vector must go through the position of the station in ECI coordinates (X'_k, Y'_k, Z'_k). For N stations, there are a total of $\binom{N}{2}$ combinations of different plane intersections. Although Ceplecha (1987) shows how to compute the weighted average trajectory for all combinations of planes, we follow the approach of Gural (2012), where only the solution with the pair of planes that have the highest convergence angle is taken. This solution is usually satisfactory to estimate the initial estimate of the trajectory for the LoS method that is then refined numerically.

For every pair of planes, we have their normals, $\hat{\boldsymbol{n}}_{\mathrm{A}}$ and $\hat{\boldsymbol{n}}_{\mathrm{B}}$, and position vectors for every station, $\boldsymbol{p}_{\mathrm{A}} = [X'_{\mathrm{A}}, Y'_{\mathrm{A}}, Z'_{\mathrm{A}}]$ and $\boldsymbol{p}_{\mathrm{B}} = [X'_{\mathrm{B}}, Y'_{\mathrm{B}}, Z'_{\mathrm{B}}]$. The convergence angle Q_{AB} between the two planes is

$$\cos Q_{AB} = \hat{\boldsymbol{n}}_{\mathrm{A}} \cdot \hat{\boldsymbol{n}}_{\mathrm{B}}. \tag{11}$$

The apparent radiant unit vector based on these two stations is

$$\boldsymbol{R} = \hat{\boldsymbol{n}}_{\mathrm{A}} \times \hat{\boldsymbol{n}}_{\mathrm{B}},$$

$$\hat{\boldsymbol{R}} = \frac{\boldsymbol{R}}{|\boldsymbol{R}|}. \tag{12}$$

We also make sure that the radiant vector is pointing in the correct direction:

$$\hat{\boldsymbol{R}} = \begin{cases} -\hat{\boldsymbol{R}}, & \text{if } [\xi_{\mathrm{A}1}, \eta_{\mathrm{A}1}, \zeta_{\mathrm{A}1}] \cdot \hat{\boldsymbol{R}} < [\xi_{\mathrm{A}n}, \eta_{\mathrm{A}n}, \zeta_{\mathrm{A}n}] \cdot \hat{\boldsymbol{R}}, \\ \hat{\boldsymbol{R}}, & \text{otherwise}, \end{cases} \tag{13}$$

where $[\xi_{\mathrm{A}1}, \eta_{\mathrm{A}1}, \zeta_{\mathrm{A}1}]$ is the vector pointing to the first observed point on the meteor trajectory from station A and $[\xi_{\mathrm{A}n}, \eta_{\mathrm{A}n}, \zeta_{\mathrm{A}n}]$ is the vector pointing to the last observed point from station A. This condition follows from the fact that the radiant is always closer to the first observed point.

The equatorial coordinates of the radiant are given by

$$\delta = \arcsin \hat{R}_z,$$

$$\alpha = \mathrm{atan2}(\hat{R}_y, \hat{R}_x) \bmod 2\pi, \tag{14}$$

where the mod2π operation wraps the right ascension to the $[0, 2\pi]$ range.

The intersection of the planes from each station forming the radiant line in 3D space is now known and unit vectors from each station to the closest point on the radiant line to the respective station can be calculated as

$$\boldsymbol{w} = \hat{\boldsymbol{R}} \times \hat{\boldsymbol{n}},$$

$$\hat{\boldsymbol{w}} = \frac{\boldsymbol{w}}{|\boldsymbol{w}|},$$

$$\hat{\boldsymbol{w}} = \begin{cases} -\hat{\boldsymbol{w}}, & \text{if } \hat{\boldsymbol{w}} \cdot [\xi_1, \eta_1, \zeta_1] < 0, \\ \hat{\boldsymbol{w}}, & \text{otherwise}. \end{cases} \tag{15}$$

The last equation ensures the vector is pointing from the station towards the radiant line. These vectors, $\hat{\boldsymbol{w}}_{\mathrm{A}}$ and $\hat{\boldsymbol{w}}_{\mathrm{B}}$, are calculated for both stations.

The range vectors from each station to the radiant line can be found as

$$\Delta\boldsymbol{p} = \boldsymbol{p}_{\mathrm{A}} - \boldsymbol{p}_{\mathrm{B}},$$

$$\cos\omega = \hat{\boldsymbol{w}}_{\mathrm{A}} \cdot \hat{\boldsymbol{w}}_{\mathrm{B}},$$

$$\boldsymbol{r}_{\mathrm{A}} = \frac{\cos\omega(\Delta\boldsymbol{p} \cdot \hat{\boldsymbol{w}}_{\mathrm{B}}) - \Delta\boldsymbol{p} \cdot \hat{\boldsymbol{w}}_{\mathrm{A}}}{1 - \cos^2\omega}\hat{\boldsymbol{w}}_{\mathrm{A}},$$

$$\boldsymbol{r}_{\mathrm{B}} = \frac{\Delta\boldsymbol{p} \cdot \hat{\boldsymbol{w}}_{\mathrm{B}} - \cos\omega(\Delta\boldsymbol{p} \cdot \hat{\boldsymbol{w}}_{\mathrm{A}})}{1 - \cos^2\omega}\hat{\boldsymbol{w}}_{\mathrm{B}}, \tag{16}$$

where $\boldsymbol{r}_A$ and $\boldsymbol{r}_B$ are vectors pointing from the stations to the respective point on the radiant line closest in range to the station.

The ECI coordinates of the position portion of the state vector are calculated by adding the ECI position of one of the stations to the appropriate range vector. We choose station A:

$$\boldsymbol{S} = \boldsymbol{p}_A + \boldsymbol{r}_A. \tag{17}$$

The trajectory solution from these two stations alone is thus represented by the apparent radiant unit vector $\hat{\boldsymbol{R}}$ and the reference position vector $\boldsymbol{S}$.

For the case with more than two stations, we also compute weights W_k for every station k as

$$P_a = \arccos\left(\hat{\boldsymbol{R}} \cdot \hat{\boldsymbol{w}}_k\right),$$

$$W_k = \sin^2 P_a, \tag{18}$$

where $\hat{\boldsymbol{w}}_k$ is computed from equation (15) and P_a is the perspective angle of the trajectory, namely, the angle made between the observer, the state vector, and the radiant line. In this approach, the station that observes the meteor closest to perpendicular to the trajectory is given the highest weight, while stations observing the meteor 'head on' have the lowest weights. If the perspective angle is low, small errors in meteor position measurement will propagate into large errors on the trajectory when they get projected; thus, the weight of those observations needs to be reduced. The weights are kept at unity if only two stations are used in the solution. The $\sin^2$ weighting scheme follows Ceplecha (1987), with the difference of using the perspective angle instead of the convergence angle. The weighting is only used for the LoS method described below.

3.4 Line-of-sight method

After pairing all planes and finding the solution with the best convergence angle, the resulting vectors $\hat{\boldsymbol{R}}$ and $\boldsymbol{S}$ are taken as the starting solution for the LoS method. This method seeks to find a radiant line (a line in 3D space) that minimizes the angular differences between all observation sightlines and the radiant line.

Let $\boldsymbol{d}_{\mathrm{obs}_{kj}} = [\xi_{kj}, \eta_{kj}, \zeta_{kj}]$ be the direction vector of every measurement from station k and $\boldsymbol{d}_{\mathrm{mod}_{kj}}$ be the direction of the modelled radiant line as seen from that station. The trajectory solution is then $\hat{\boldsymbol{R}}$ and $\boldsymbol{S}$ for which

$$\min \frac{\sum_{k=1}^{N_{\mathrm{stations}}} \sum_{j=1}^{N_{\mathrm{meas}(k)}} W_k \angle(\hat{\boldsymbol{d}}_{\mathrm{obs}_{kj}}, \hat{\boldsymbol{d}}_{\mathrm{mod}_{kj}})}{\sum_{k=1}^{N_{\mathrm{stations}}} W_k}. \tag{19}$$

This sum is minimized numerically using the Nelder–Mead method. $\hat{\boldsymbol{d}}_{mod_{kj}}$ can be calculated using

$$\boldsymbol{d}_{\mathrm{mod}_{kj}} = \boldsymbol{T}'_{kj} - \boldsymbol{p}_{kj},$$

$$\hat{\boldsymbol{d}}_{\mathrm{mod}_{kj}} = \frac{\boldsymbol{d}_{\mathrm{mod}_{kj}}}{|\boldsymbol{d}_{\mathrm{mod}_{kj}}|}, \tag{20}$$

where $\boldsymbol{T}'_{kj}$ is the gravity-corrected point on the radiant line that is the closest to the measured line of sight and $\boldsymbol{p}_{kj}$ are the ECI coordinates of station k at time j. $\boldsymbol{T}'_{kj}$ can be computed as

$$\boldsymbol{T}'_{kj} = \boldsymbol{T}_{kj} - \Delta h(t_{kj}) \frac{\boldsymbol{T}_{kj}}{|\boldsymbol{T}_{kj}|}, \tag{21}$$

where $\boldsymbol{T}_{kj}$ is a point on the radiant line that is the closest to the measured line of sight that can be computed using equations given in Appendix B. Δh is the height drop due to gravity computed using the equations in Appendix A; adding this term effectively simulates the curvature of the trajectory due to gravity. t_{kj} here is the time the meteor is at point j as seen from station k relative to $\mathrm{JD}_{\mathrm{ref}}$.

The angle between the closest point on the 3D radiant line and the observed line of sight is calculated as (note that unit vectors must be used)

$$\angle(\hat{\boldsymbol{d}}_{\mathrm{obs}_{kj}}, \hat{\boldsymbol{d}}_{\mathrm{mod}_{kj}}) = \arccos\left(\hat{\boldsymbol{d}}_{\mathrm{obs}_{kj}} \cdot \hat{\boldsymbol{d}}_{\mathrm{mod}_{kj}}\right). \tag{22}$$

3.5 Computing meteor length, velocity, and lag

Once a trajectory solution is found, the location of the estimated reference state vector position $\boldsymbol{S}$ along the radiant line is moved to the beginning of the meteor. This is done by setting $\boldsymbol{S}$ to the ECI coordinates on the radiant line with the largest observed height, implicitly assuming that a meteor is always descending downward (not necessarily true for Earth-grazers).

The length along the track is found by projecting the observations on the radiant line using the equations given in Appendix B, producing $\boldsymbol{d}_{\mathrm{mod}_{kj}}$. The meteor length is defined as the distance from the reference state vector position $\boldsymbol{S}$ to every projected measurement ray along the radiant line:

$$l_{kj} = |\boldsymbol{d}_{\mathrm{mod}_{kj}} - \boldsymbol{S}|. \tag{23}$$

The time variation of velocity defines deceleration, but since it is the second derivative of the length versus time, deceleration itself tends to have large point-to-point variances. As a proxy for overall deceleration, we use lag. Following Subasinghe, Campbell-Brown & Stokan (2017), we define lag as 'the distance that the meteoroid falls behind an object with a constant velocity that is equal to the initial meteoroid velocity'. In that work, the authors use the first half of the meteor's trajectory to estimate the initial velocity. The limitation of this approach is that the time offsets between observations from different stations can cause errors if all observations from all sites are simultaneously used for the velocity estimation. Thus, the time offsets have to be estimated first.

3.6 Estimating timing offsets and the initial velocity

To estimate timing offsets, we use the fact that the computed length is insensitive to offsets in time. The timing offset estimation is performed by using the station that first recorded the meteor as the station with reference time for all other stations; i.e. it has absolute time ($\Delta t = 0$). The time offsets for all stations are then numerically estimated by minimizing the sum of time differences for all combinations of station pairs. The minimization cost function $f_{\Delta t}$ is defined as

$$f_{\Delta t} = \frac{t_{\mathrm{sum}}}{W_{\mathrm{sum}} c_{\mathrm{sum}}},$$

$$t_{\mathrm{sum}} = \sum_{k=1}^{N_{\mathrm{stations}}} \sum_{r=1}^{N_{\mathrm{stations}}} \sum_{j=1}^{N_{\mathrm{meas}(r)}} W_k W_r \left(t_k(l_{rj}) - t_{rj}\right)^2,$$

$$W_{\mathrm{sum}} = \sum_{k=1}^{N_{\mathrm{stations}}} \sum_{r=1}^{N_{\mathrm{stations}}} W_k W_r,$$

$$c_{\mathrm{sum}} = \sum_{k=1}^{N_{\mathrm{stations}}} \sum_{r=1}^{N_{\mathrm{stations}}} N_{\mathrm{overlap}}, \tag{24}$$

where k is the station index, r the index of all other stations (iterations where $k = r$ are skipped), t_{rj} is the time from station r, and $t_k(l_{rj})$ is the time from station k at length from station r. $t_k(l_{rj})$

is obtained by linear interpolation of time versus length. W_k and W_r are weights for the respective stations as defined in equation (18), and N_{overlap} is the number of points that overlap in length between stations k and r. Thus, only overlapping segments of the meteor path for stations k and r are used. This requirement is the main limitation of the method: for the approach to work, an overlap of at least four points between stations is needed. If there is no overlap (e.g. one station observed only the beginning and the other only the end of a meteor), the approach will not work and one has to assume a velocity model. For those cases, we found that the MPF method of Gural (2012) worked well.

This approach of estimating time offsets is not sensitive to the functional form of the deceleration; it relies on that fact that a truly accurate trajectory solution must show the same dynamics from all stations. If the observed dynamics differ, it indicates that the trajectory was not well estimated. This is the central foundation of our novel approach.

After an initial estimate is made of the timing offsets, the entire trajectory solution is repeated with updated timing offsets. JD_{ref} is shifted to correspond to the new value of $t = 0$. Because the state vector $\boldsymbol{S}$ is kept at the beginning of the meteor, this means that the position of the meteor at time JD_{ref} corresponds to $\boldsymbol{S}$.

The initial velocity is then estimated by progressively fitting a line to the solution time versus length. This is done starting from the first 25 per cent of points from all stations (at least four points for short events) up to 80 per cent of all points. The best estimate of the initial velocity is the fit with the smallest standard deviation.

This modification mitigates the influence of deceleration on the initial velocity estimate, although at best it is the average velocity of the first 25 per cent of the trajectory. In practice, we found that this approach works well. This approach was adopted because the standard deviation of the fit done on the first quarter of the trajectory is usually high due to the measurement uncertainty as meteors tend to be faint at the beginning of the trail and thus the initial velocity may be uncertain as well. As more points get included, the standard deviation tends to go down, but it will rise again if significant deceleration is present. The approach is thus a balance between choosing a fit that trades the effects of measurement uncertainty and deceleration.

To demonstrate the accuracy of the method, we have simulated a Draconid as it would be observed by a hypothetical network in Southern Ontario consisting of three stations with FOVs of $64^\circ \times 48^\circ$ that form an equilateral triangle with sides of 100 km and observe the same volume of the sky (maximum overlap at height of 100 km; see the second paper for more simulation details). The accuracy of measurements was $\sigma = 0.5$ arcmin.

Fig. 2 shows the map of these model stations and the trail of the meteor. The left inset of Fig. 3 shows time versus length prior to the timing correction. One can see that all observations show the same trend (i.e. dynamics), but they are only offset in time. The right inset shows the lengths after estimating timing offsets and the final fitted initial velocity. Note that the observations start deviating slightly from the fitted velocity line at the end, indicating significant deceleration.

The effect is more visible in Fig. 4 that shows the computed lag. Ideally, the lag would remain zero (a vertical line) until the meteor starts decelerating, and that straight portion would be used for initial velocity estimation. This may not always be the case if the deceleration started prior to detection, as shown in the aforementioned figure. In that case, the initial velocity will be underestimated and ablation modelling is needed to reconstruct the true initial velocity (Vida et al. 2018b). Also, notice the larger

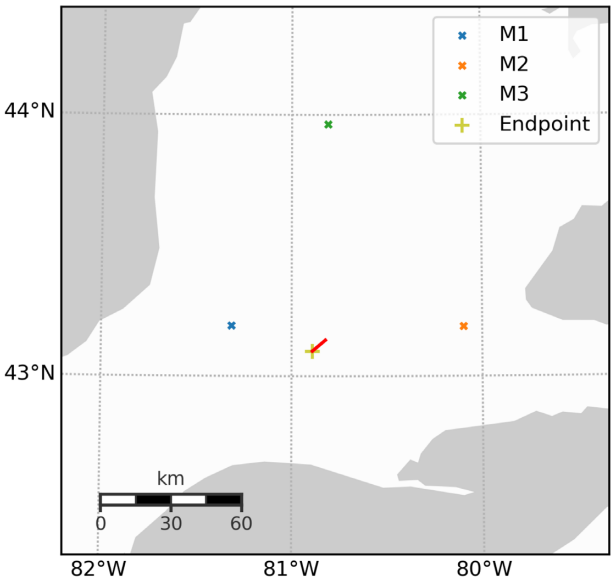

Figure 2. Map of the hypothetical moderate FOV network and the simulated Draconid of mass 6.45×10^{-5} kg, density 211 kg m^{-3}, and initial velocity 23.7 km s^{-1}. The meteor had an entry angle of 65°. Perspective angles for stations M1, M2, and M3 were 19°, 53°, and 61°, respectively. The red line represents the ground track of the meteor.

scatter in lag and fit residuals (Fig. 5) from station M1 due to the low perspective angle of only 19°. The perspective angles of the other two stations M2 and M3 are 53° and 61°, respectively.

Finally, after the reference state vector, the radiant, and the initial velocity are known, the orbit is computed using equations given in Appendix C.

3.7 Refining the trajectory solution – a Monte Carlo approach

With a nominal trajectory solution now available, the next goal is to define uncertainties in the solution and further optimize the solution using time versus length consistency as the cost function metric.

After estimating the initial 'best' solution as described earlier, the angular residuals of observations from all stations relative to this solution are computed using equation (22), as well as the value of the root-mean-square deviation (RMSD). We assume that the computed RMSD represents the standard deviation of the real (random) measurement uncertainty of individual stations.

Fig. 5 shows the computed angular residuals for the example meteor in Fig. 4. Note that station M1 has the highest RMSD, again due to its low perspective angle. In this case, a low station weight will prevent these measurements from significantly influencing the trajectory solution.

Next, Gaussian noise is added to the original measurements from every station (using equation 36), with a standard deviation estimated from the measured station residuals. The entire trajectory is then recomputed from the beginning and a new positional state vector, radiant, velocity, and orbit are computed using the noise-added data. This procedure is repeated hundreds of times with randomized noise injected into every run.

The best solution is chosen as the one with the smallest value of the $f_{\Delta t}$ function (equation 24). This solution is the one where the most consistent dynamics of a meteor have been observed across all stations and which is simultaneously consistent within measurement uncertainty from all stations. This produces the best dynamical solution within the geometrical uncertainty.

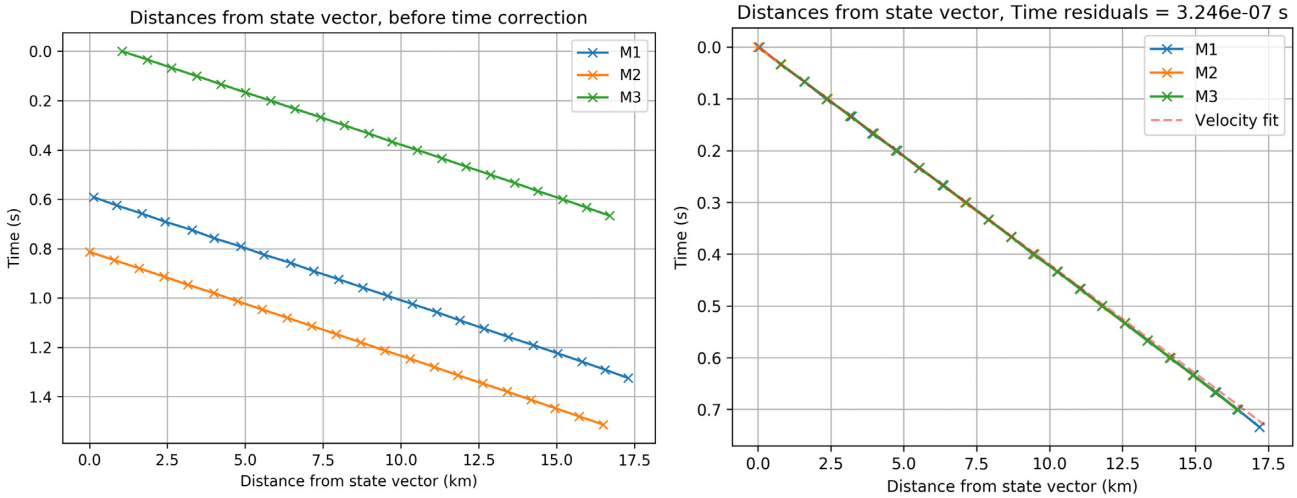

Figure 3. *Left:* Time versus length before correction. *Right:* After time offset estimation, all curves are one on top of the other. The cited residual is the average residual between all lines in seconds.

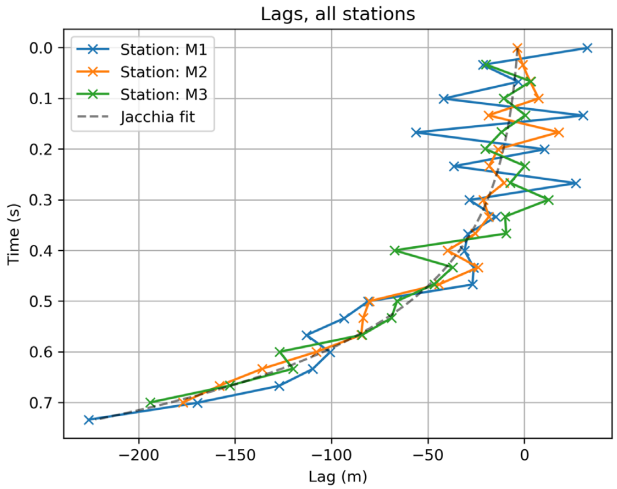

Figure 4. A lag of a simulated Draconid observed by a moderate FOV system from three stations. 'Jacchia fit' is a fit of equation (3) to the computed lag.

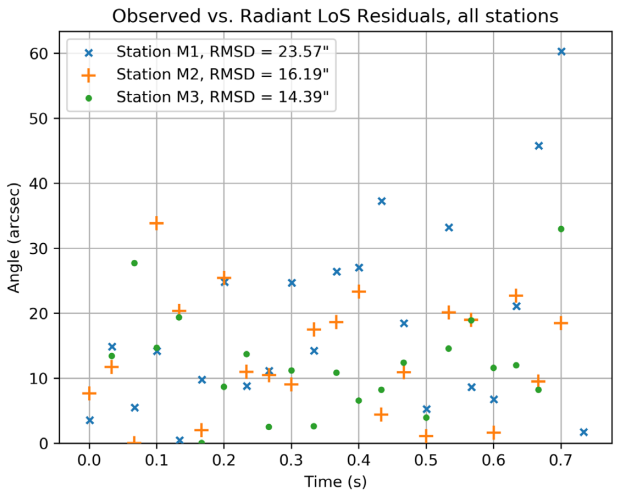

Figure 5. Angular residuals of a simulated Draconid. RMSD is the root-mean-square deviation in arcseconds.

In many cases when the geometry is good and the measurements are reasonably precise, the Monte Carlo refinement will not provide additional improvement beyond the initial solution. The comparison of the performance of the Monte Carlo solver to other trajectory solvers on simulated data is given in the second paper in this series.

The measurement uncertainty of every estimated parameter (including the orbital parameters) is computed using the subset of Monte Carlo trajectories that have values of the $f_{\Delta t}$ function smaller than that of the initial purely geometrical solution. If all solutions were to be used for uncertainty estimation, then the uncertainties would be completely driven by geometric uncertainties. This culling removes all solutions that have worse fits to the dynamics between stations than the geometrical solution; thus, the dynamical constraints are included. Note that this approach does not estimate possible systematic errors arising from the astrometric calibration and position picks, which are system dependent and should be handled separately.

Fig. 6 shows the geocentric radiants of all Monte Carlo solutions (the value of the square root of the $f_{\Delta t}$ function is colour coded), and Fig. 7 shows how the geocentric velocity varies with the radiant position for the example model Draconid meteor. Fig. 8 shows the spread in orbital elements, in particular the strong dependence of individual orbital elements on one another. This behaviour is not captured simply by describing independently computing standard deviations of every orbital element.

To more realistically convey trajectory and orbital uncertainties, we compute covariance matrices of both the orbit and the initial state vector. Note that the uncertainty in the geocentric radiant is not properly represented by considering standard deviations in the right ascension and declination separately. Most two-station meteor events, particularly those with a low convergence angle, show an elongated radiant uncertainty. Using a different model Draconid, just such an example is shown in Fig. 9.

Note that Fig. 6 shows a clear correlation of the timing residuals (the $f_{\Delta t}$ function) relative to radiant position and a clear global minimum. In experimentation with model fits, we have found this behaviour to be a strong indicator of an improvement in the trajectory solution relative to the geometrical best solution, showing that the best Monte Carlo trajectory should be taken as the solution with lowest lag residuals.

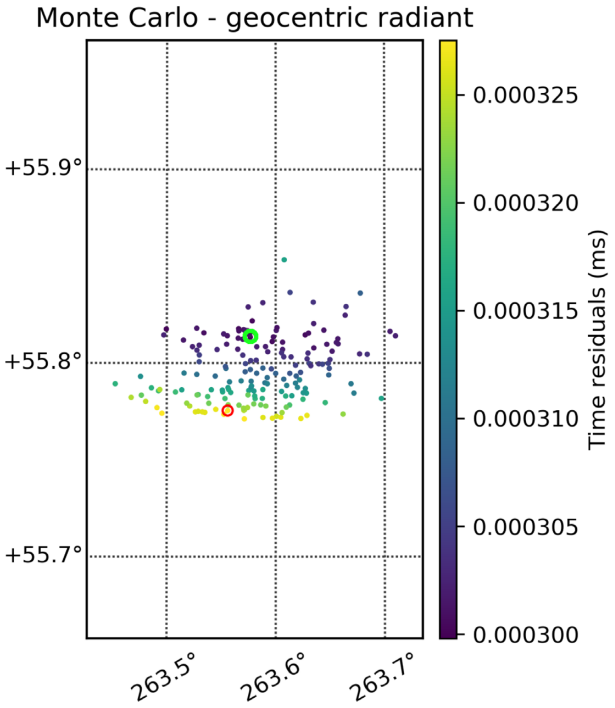

Figure 6. Spread in the geocentric radiant of the model Draconid. The square root of the timing residual $f_{\Delta t}$ is colour coded. The red circle marks the position of the initial solution $f_{\Delta t} = 0.000\,326$ and the green circle marks the position of the best solution $f_{\Delta t} = 0.000\,300$.

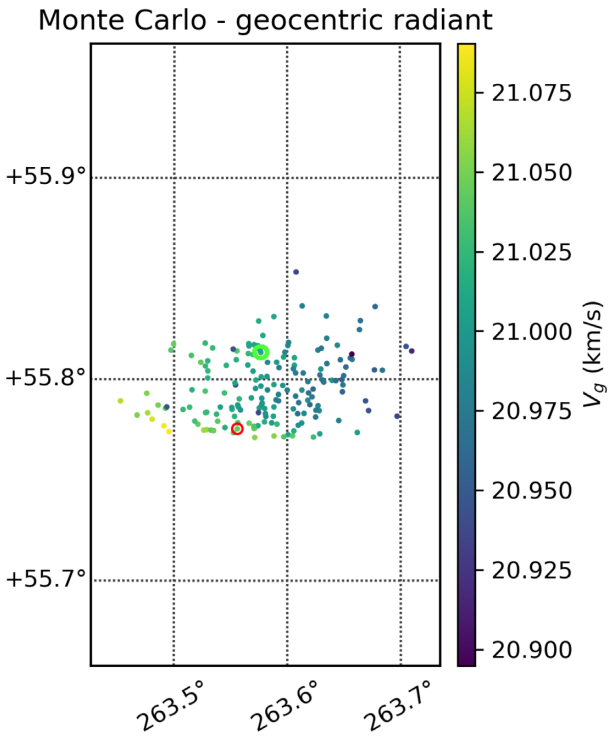

Figure 7. Spread in the geocentric radiant for the modelled Draconid; the geocentric velocity is colour coded. The red circle marks the position of the initial solution ($V_g = 21.05\,\mathrm{km\,s^{-1}}$) and the green circle marks the position of the best solution ($V_g = 21.00\,\mathrm{km\,s^{-1}}$).

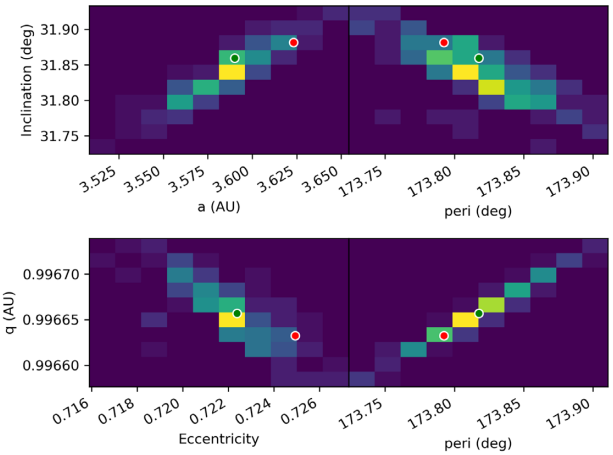

Figure 8. 2D histogram of the spread in orbital elements for the modelled Draconid. The red circle marks the position of the initial solution and the green circle marks the position of the best solution. Brighter bins indicate more trials within the bin.

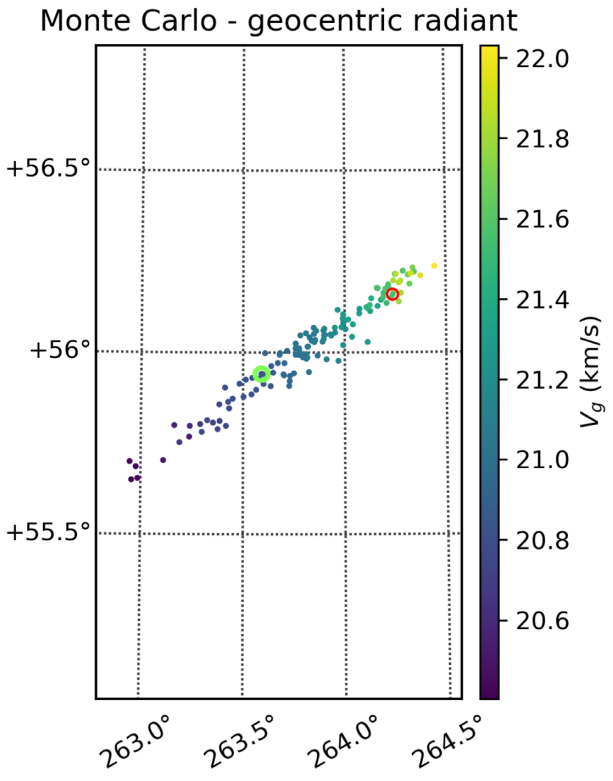

Figure 9. A separate simulation done to illustrate how elongated the radiant uncertainty can be. Here, the geocentric velocity is colour coded. The red circle marks the position of the initial (geometrical) solution and the green circle marks the position of the best (lowest lag cost function) solution. The original model input value of the geocentric velocity was $V_g = 20.893\,\mathrm{km\,s^{-1}}$. The initial LoS solution underestimated the velocity by $\Delta V_g = -0.661\,\mathrm{km\,s^{-1}}$, while the Monte Carlo method slightly overestimated by only $\Delta V_g = 0.017\,\mathrm{km\,s^{-1}}$.

We note that for some model geometries, there are cases when no consistent gradient in the residuals with radiant location is present. In these cases, the values of the $f_{\Delta t}$ function are randomly scattered among radiant solutions. In such cases, we found that keeping the original purely geometric solution produced fits closer to the simulated trajectory.

4 METEOR SHOWER AND TRAJECTORY SIMULATOR

By developing a comprehensive meteor trajectory simulator, we wish to generate synthetic measurements for specific video systems in realistic conditions. This involves generating model observations by stipulating real locations of meteor stations, instrument FOVs, cadence, sensitivity, and measurement uncertainties. In this work, we require the simulator to produce simulated trajectories of shower meteors, but sporadic meteors can also be simulated given a sporadic source model. Meteor showers are simulated by specifying the radiant, radiant drift, and radiant spread (assumed to be Gaussian), in addition to an activity profile.

The dynamics of the meteor's motion within the model are generated using the meteor ablation model of Campbell-Brown & Koschny (2004) for which the range of meteoroid masses, the mass index, the meteoroid bulk density distribution, and the ablation coefficient are defined as inputs. The attraction of the meteoroid body to the Earth's centre due to gravity is taken into account as well. Higher order gravitational coefficients are disregarded because their influence is not measurable using these methods. In what follows, we describe the details of the simulator and demonstrate that it produces meteor trajectories comparable to real observations. The trajectory simulator outputs sets of time, right ascension, declination, and apparent magnitude for every simulated meteor, emulating what would be seen by observers on the ground.

4.1 Simulating radiants and activity

For each model station, the following parameters are defined:

(i) The geographical coordinates: longitude λ, geodetic latitude φ, and elevation above a WGS84 geoid of the Earth h.

(ii) The sensor system parameters:

(a) cadence [i.e. frames per second (FPS) of the video camera];

(b) maximum possible deviation in time ($\Delta t_{\max}$) from the absolute time;

(c) azimuth A and altitude a of the FOV centre for each local site coordinates;

(d) width and height of the rectangular FOV;

(e) meteor limiting magnitude MLM;

(f) radiant power of a zero-magnitude meteor $P_{0\mathrm{m}}$ (see Ayers 1965).

For each station, the time offset from the absolute time and asynchronous timing shift between cameras is drawn from a uniform distribution $U(0, \Delta t_{\max})$. The time offset and video frame rate are assumed constant over the duration of the meteor. The measurement precision of leading edge picks along the meteor track is simulated by adding Gaussian noise to each simulated measurement with a standard deviation equal to the scatter in residuals for real measurements.

To make the resulting trajectory solution averages per shower have realistic weighted geometries given the station locations, activity profiles for each shower are required. The activity profile of simulated meteor showers is defined by the solar longitude of the peak $\lambda_{\odot}^{\max}$ and the slope of the activity profile B, where the activity is approximated as $\mathrm{ZHR} = \mathrm{ZHR}_{\max} 10^{-B|\lambda_{\odot} - \lambda_{\odot}^{\max}|}$ following Jenniskens (1994). The activity profile is assumed to be symmetric with respect to the peak. N samples are drawn from the activity profile using the inverse sampling transform method – every sample represents one simulated meteor. First, N samples are drawn from a uniform distribution $U(0, 1)$, producing a vector $(y_1, \ldots, y_N)$. Next, signs are drawn from a uniform distribution $U(-1, 1)$, producing a vector $(s_1, \ldots, s_N)$. The solar longitude of each sample is then computed as

$$\lambda_{\odot i} = \lambda_{\odot}^{\max} + \mathrm{sgn}(s_i)\frac{\log_{10} y_i}{B}, \tag{25}$$

and only those simulated shower meteors having solar longitudes that occurred between the local astronomical twilight and dawn of all observers are used.

Simulated meteor shower radiants are defined by their geocentric right ascension α_{g} and declination δ_{g} taken to be the mean radiant at the peak together with the standard deviation of the radiant dispersion $\sigma_{\alpha}, \sigma_{\delta}$. For times away from the peak, the radiant drifts Δ_{α} and Δ_{δ} in degrees on the sky per degree of solar longitude are used. The shower geocentric velocity V_{g} and speed dispersion $\sigma_{V_{\mathrm{g}}}$ plus drift $\Delta_{V_{\mathrm{g}}}$ (if known) are also assigned.

N of individual meteor radiant realizations are drawn from a von Mises distribution (a close approximation to the circular normal distribution) using the centre of distribution at $\mu = 0$ and the dispersion parameter $\kappa = 1/\sigma^2$. α and δ are drawn independently. This procedure produces vectors $(\alpha'_1, \ldots, \alpha'_N)$ and $(\delta'_1, \ldots, \delta'_N)$. These vectors are offsets in right ascension and declination from the mean radiant position. To compute the proper distribution of radiants on the celestial sphere centred around $(\alpha_{\mathrm{g}}, \delta_{\mathrm{g}})$, the unit vector $\hat{\boldsymbol{R}}_{\mathrm{g}} = (1, 0, 0)$ is rotated by $-\delta'_i$ on the Y-axis, and then by α'_i on the Z-axis for every coordinate pair i. Next, the resulting vector is rotated by the negative declination of the mean radiant $-\delta_{\mathrm{g}}$ on the Y-axis, and then by α_{g} on the Z-axis, and converted to right ascension and declination:

$$\begin{aligned} \alpha_{gi} &= \mathrm{atan2}\left(\hat{R}_{giy}, \hat{R}_{gix}\right), \\ \delta_{gi} &= \arcsin \hat{R}_{giz}. \end{aligned} \tag{26}$$

The radiant drift is applied as

$$\begin{aligned} \alpha_{gi} &= \alpha_{gi} + \Delta_{\alpha}\left(\lambda_{\odot i} - \lambda_{\odot}^{\max}\right), \\ \delta_{gi} &= \delta_{gi} + \Delta_{\delta}\left(\lambda_{\odot i} - \lambda_{\odot}^{\max}\right). \end{aligned} \tag{27}$$

Geocentric velocities V_{gi} are drawn from a Gaussian distribution $N(V_{\mathrm{g}}, \sigma_{V_{\mathrm{g}}})$, and a drift in V_{g} is applied as

$$V_{gi} = V_{gi} + \Delta_{V_{\mathrm{g}}}\left(\lambda_{\odot i} - \lambda_{\odot}^{\max}\right). \tag{28}$$

4.2 Generating meteor state vectors and apparent radiants

The beginning of the luminous flight of the meteor is used as the point of reference (i.e. instantaneous measurement of the state vector). This point is randomly generated to be inside the FOVs of at least two stations in the simulation for a given start height. We use a start height of 120 km as a reference point between the trajectory and the ablation model. 120 km was chosen because almost no meteors end above this height, so the reference point on the trajectory is before or during the luminous phase.

The following paragraphs describe the procedure for generating initial meteor position vectors in 3D space.

Four rays representing the four corners of the FOV of one camera emanate from the coordinates of the station (equivalent to the centre of the sensor focal plane). ECI coordinates are used. A frustum (truncated pyramid) is obtained by taking eight points in total, each lying on an FOV corner ray at heights −5 and +5 km around the simulated beginning height for a particular meteor. A random point is generated inside the frustum of one station, and this random sampling is repeated until the point is inside a frustum of at least one another station. The overlap is checked using the quickhull algorithm (Barber, Dobkin & Huhdanpaa 1996). The resulting 3D position vector $\boldsymbol{S}$ is taken to be the beginning point of the simulated meteor in ECI coordinates. All initial positions are generated inside overlapping FOVs of at least two cameras due to the computational simplicity of the approach.

From this initial point and the given geocentric radiant, the apparent radiant and the initial velocity are computed in the ECI frame. The initial velocity v_0 ($\mathrm{m\,s^{-1}}$) is computed from the inverse of the geocentric velocity equation (7) in Appendix C2:

$$v_0 = \sqrt{v_g^2 + \frac{2 \times 6.674\,08 \times 5.9722 \times 10^{13}}{|\boldsymbol{S}|}} \tag{29}$$

and the apparent values of the radiant (α_i, δ_i) are numerically inverted using forward mapping equations (see Appendix C2). The apparent radiant unit vector $\hat{\boldsymbol{R}}$ is computed by converting the spherical coordinates (α_i, δ_i) to their ECI components using equation (5). Note that v_g is converted into the initial velocity by assuming that the stations are moving in the ECI coordinates, and thus the whole coordinate system rotates with the Earth, making a correction to the meteor velocity for Earth's rotation unnecessary; such a correction would be needed for an ECEF treatment. Radiants with zenith angles $z_c > 80^\circ$ are skipped to avoid simulating meteors that do not propagate down in the atmosphere.

4.3 Simulating meteoroid dynamics

To simulate realistic meteor dynamics, the meteoroid ablation model of Campbell-Brown & Koschny (2004) is used. For each shower, a range of visible masses $m_{\min}$, $m_{\max}$ and a mass index s based on literature values for a particular shower are defined. The masses are sampled using inverse transform sampling from the cumulative number as a function of mass distribution:

$$f(m) = m^{1-s}. \tag{30}$$

Meteoroid densities are sampled uniformly either from a user-defined range or using density distributions given by Moorhead et al. (2017). The apparent ablation coefficient σ (usually given in $\mathrm{s^{-2}\,km^{-2}}$) is applied in the ablation model through modification of the energy needed to ablate a unit mass L ($\mathrm{J\,kg^{-1}}$; make sure to convert σ to $\mathrm{s^{-2}\ m^{-2}}$), which is computed as

$$L = \frac{\Lambda}{2\sigma\Gamma}, \tag{31}$$

where $\Lambda = 0.5$ is the heat transfer coefficient and $\Gamma = 1.0$ is the drag coefficient. Note that in the field of aerodynamics the notation C_d is used for the drag coefficient, where $\Gamma = 2C_d$. The ablation model provides vectors of height, length, and luminosity along the meteor path from the beginning point with a temporal resolution of 0.001 s. Note that σ is used throughout the text with different meanings. In equation (31), it is used for the ablation coefficient, while at all other places it is used for standard deviation.

4.4 Generating synthetic trajectory data

The duration t_{meteor} of a meteor is obtained from the ablation model. We assume that the beginning time $t = 0$ corresponds to a given solar longitude for the corresponding reference Julian date $\mathrm{JD_{ref}}$. A vector of times is obtained by sampling the range (0, t_{meteor}) with the step 1/FPS.

The instantaneous model luminosity I at a given time is converted to a range-corrected apparent magnitude M_v and only those points above the meteor limiting magnitude of individual stations are taken:

$$M_A = -2.5 \log_{10} \frac{I}{P_{0m}},$$

$$M_v = M_A - 5 \log_{10} \frac{10^5}{r}, \tag{32}$$

where M_A is the absolute magnitude (magnitude at 100 km range) and r is the range in metres from the station to the meteor. P_{0m} is the power of a zero-magnitude meteor for the appropriate bandpass taken from Weryk & Brown (2013). No correction for angular velocity or extinction loss is included.

The 3D meteor positions are projected to local spherical coordinates of stations to generate synthetic observations. We simulate the real movement of the stations due to Earth's rotation by computing ECI coordinates $\mathbf{ECI}_j$ of stations at every model point in time t_k. The position of the meteor in ECI coordinates at time t_j is computed as

$$\boldsymbol{T}_j = \boldsymbol{S} - d(t_j)\hat{\boldsymbol{R}}, \tag{33}$$

where $\boldsymbol{S}$ is the initial position at $t = 0$ and $\hat{\boldsymbol{R}}$ is the apparent radiant unit vector in ECI coordinates. The additional decrease in height due to Earth's gravity is applied using equation (21), where $\Delta h(t_j)$ is the decrease in height at every point in time due to gravity since the beginning (in metres). This procedure simulates the curvature of the trajectory due to gravity, assuming the pull is perpendicular to the WGS84 reference ellipsoid. $\Delta h(t_j)$ is computed as described in Appendix A. A unit vector pointing from the station to the position of the meteor on the trajectory is computed as

$$\hat{\boldsymbol{r}} = \frac{\boldsymbol{T}_j - \mathbf{ECI}_j}{|\boldsymbol{T}_j - \mathbf{ECI}_j|}. \tag{34}$$

We simulate the observational precision of a system by adding Gaussian noise with a standard deviation σ, derived from real measurements of the actual systems, to the synthetic observations. We separate the vector $\hat{\boldsymbol{r}}$ into orthogonal components $\hat{\boldsymbol{u}}$ and $\hat{\boldsymbol{v}}$:

$$\hat{\boldsymbol{z}} = [0, 0, 1],$$

$$\hat{\boldsymbol{u}} = \frac{\hat{\boldsymbol{r}} \times \hat{\boldsymbol{z}}}{|\hat{\boldsymbol{r}} \times \hat{\boldsymbol{z}}|},$$

$$\hat{\boldsymbol{v}} = \frac{\hat{\boldsymbol{u}} \times \hat{\boldsymbol{r}}}{|\hat{\boldsymbol{u}} \times \hat{\boldsymbol{r}}|}. \tag{35}$$

The direction vector (all in ECI) with the added noise is then

$$\boldsymbol{r}' = \hat{\boldsymbol{r}} + \mathcal{N}(0, \sigma)\,\hat{\boldsymbol{u}} + \mathcal{N}(0, \sigma)\,\hat{\boldsymbol{v}}, \tag{36}$$

where $\mathcal{N}(0, \sigma)$ is a scalar drawn from a Gaussian distribution with a mean of 0 and a standard deviation of σ. The samples are drawn separately for each term. The direction vector is converted to

equatorial coordinates in the epoch of date:

$$\hat{\boldsymbol{r}}' = \frac{\boldsymbol{r}'}{|\boldsymbol{r}'|},$$

$$\alpha_j = \text{atan2}\left(\hat{r}'_y, \hat{r}'_x\right),$$

$$\delta_j = \arcsin \hat{r}'_z. \tag{37}$$

Finally, the appropriate timing offset Δt for a given station (randomized on a per meteor basis) is added to time t_j, completing the set of synthetic measurements for each simulated meteor.

At the end of this procedure, one obtains a set of N_{meas} synthetic measurements from every station for every generated meteor. Synthetic meteors are uniquely defined by the Julian date of their beginning JD_{ref}, set of relative times since the beginning $(t_0, \ldots, t_j)$, a set of right ascensions $(\alpha_0, \ldots, \alpha_j)$ and declinations $(\delta_0, \ldots, \delta_j)$ in the epoch of date. Note that the epoch here is not J2000; to avoid confusion, we convert the model measurements to local azimuth $(A_0, \ldots, A_j)$ and altitude $(a_0, \ldots, a_j)$ in the epoch of date from a particular station using equations given in Appendix F.

Although the simulator reproduces many features of the observed data, a major difference with real meteors is that synthetic trajectories all start within the FOVs of at least two stations. It is not clear that this limitation is significant for the current work. While this might be alleviated by generating the state vectors slightly outside the FOV of one camera, this would be at the expense of having to compute the propagation as well, which would significantly increase the computational load of finding a synthetic meteor that is actually visible from two or more stations.

5 CONCLUSION

A novel Monte Carlo meteor trajectory method was developed that takes the dynamics of meteors into account without assuming any formulated meteor propagation model. This leverages the fact that modern meteor electro-optical systems have sufficient precision to routinely record deceleration, allowing an entirely independent check on the solution consistency between stations.

Improvements in weighting multistation observations as well as a new method of initial velocity estimation have been proposed. A limitation of the new Monte Carlo solver is that it does not work for meteors with no temporal overlap between stations. In those cases, a dynamical model must be used to estimate timing differences and the velocity, but the radiant and its uncertainty can be estimated using purely geometrical methods, similar to earlier approaches (Gural 2012; Weryk & Brown 2012).

We develop a meteor trajectory simulator that uses a numerical meteor ablation model to simulate meteor dynamics. The simulator will be used in the second paper in this series to investigate radiant and velocity accuracy that can be achieved for various real-world optical systems and meteor showers.

Finally, we provide a detailed set of equations and explanations for estimating meteor trajectories and computing orbits starting just from a set of multistation observations. We also have made the associated code base openly available for all to use. Additional details are included in the accompanying appendices. An improved version of the MPF method incorporating the findings of this paper will be published in the future. We invite readers to continue to the second paper in this series for results.

5.1 Note on code availability

Implementation of the meteor simulator as well as implementation of all meteor solvers used in this work are published as open source on the following GitHub web page: https://github.com/wmpg/WesternMeteorPyLib. Readers are encouraged to contact the authors in the event they are not able to obtain the code online.

ACKNOWLEDGEMENTS

We thank Dr. Eleanor Sansom for a helpful and detailed review of an earlier version of this manuscript. Also, we thank Dr. Steven Ehlert for suggesting the name 'Pylig' for the Monte Carlo trajectory solver developed as a part of this work, as well as David L. Clark for a fruitful discussion about meteor orbit computation. Funding for this work was provided by the NASA Meteoroid Environment Office under cooperative agreement 80NSSC18M0046. Peter G. Brown acknowledges funding support from the Canada Research Chairs program and the Natural Sciences and Engineering Research Council of Canada.

REFERENCES

Ayers W. G., 1965, NASA, TN D-2931
Barber C. B., Dobkin D. P., Huhdanpaa H., 1996, ACM Trans. Math. Softw., 22, 469
Borovička J., 1990, Bull. Astron. Inst. Czech., 41, 391
Borovička J., Spurnỳ P., Koten P., 2007, A&A, 473, 661
Burke J. G., 1986, Cosmic Debris: Meteorites in History. Univ. California Press, Berkeley, CA
Campbell-Brown M. D., Koschny D., 2004, A&A, 418, 751
Ceplecha Z., 1979, Bull. Astron. Inst. Czech., 30, 349
Ceplecha Z., 1987, Bull. Astron. Inst. Czech., 38, 222
Ceplecha Z., Borovička J., Elford W. G., Revelle D. O., Hawkes R. L., Porubčan V., Šimek M., 1998, Space Sci. Rev., 84, 327
Clark D. L., 2010, PhD thesis, Univ. Western Ontario, London, Ontario, Canada
Eberhart R., Kennedy J., 1995, in Proceedings of the IEEE international conference on neural networks, IEEE, Perth, WA, Australia, p. 1942
Eberly D. H., 2006, 3D Game Engine Design: A Practical Approach to Real-Time Computer Graphics. CRC Press, Boca Raton, FL
Egal A., Gural P. S., Vaubaillon J., Colas F., Thuillot W., 2017, Icarus, 294, 43
Folkner W. M., Williams J. G., Boggs D. H., Park R. S., Kuchynka P., 2014, Interplanet. Netw. Prog. Rep., 196, C1
Gural P. S., 2001, WGN J. Int. Meteor Organ., 29, 134
Gural P. S., 2012, Meteorit. Planet. Sci., 47, 1405
Hawkes R. L., Jones J., 1975, MNRAS, 173, 339
Hughes D. W., 1982, Vistas Astron., 26, 325
Jenniskens P., 1994, A&A, 287, 990
Jenniskens P., Gural P. S., Dynneson L., Grigsby B. J., Newman K. E., Borden M., Koop M., Holman D., 2011, Icarus, 216, 40
Meeus J. H., 1998, Astronomical Algorithms, 2nd edn. Willmann-Bell, Incorporated, Richmond, VA
Moorhead A. V., Blaauw R. C., Moser D. E., Campbell-Brown M. D., Brown P. G., Cooke W. J., 2017, MNRAS, 472, 3833
Pavlis N. K., Holmes S. A., Kenyon S. C., Factor J. K., 2012, J. Geophys. Res., 117
Romig M. F., 1966, Meteorit. Planet. Sci., 3, 11
Sansom E. K., Rutten M. G., Bland P. A., 2017, AJ, 153, 87
Schiaparelli G. V., von Boguslawski G., 1871, Entwurf einer astronomischen Theorie der Sternschnuppen. Th. von der Nahmer, Szczecin, Poland
Stokan E., Campbell-Brown M. D., Brown P. G., Hawkes R. L., Doubova M., Weryk R. J., 2013, MNRAS, 433, 962

Subasinghe D., Campbell-Brown M. D., Stokan E., 2016, MNRAS, 457, 1289
Subasinghe D., Campbell-Brown M. D., Stokan E., 2017, Planet. Space Sci., 143, 71
Tsuchiya C., Sato M., Watanabe J.-I., Moorhead A. V., Moser D. E., Brown P. G., Cooke W. J., 2017, Planet. Space Sci., 143, 142
Vida D., Brown P. G., Campbell-Brown M., Huggins S., 2018a, in Proc. Int. Meteor Conf., Petnica, Serbia, 21–24 September 2017, IMO, Gyssens M., Rault J.-L., p. 18
Vida D., Brown P. G., Campbell-Brown M., 2018b, MNRAS, 479, 4307
Weryk R. J., Brown P. G., 2012, Planet. Space Sci., 62, 132
Weryk R. J., Brown P. G., 2013, Planet. Space Sci., 81, 32
Weryk R. J., Campbell-Brown M. D., Wiegert P. A., Brown P. G., Krzeminski Z., Musci R., 2013, Icarus, 225, 614
Whipple F. L., Jacchia L. G., 1957, Smithsonian Contrib. Astrophys., 1, 183

APPENDIX A: BENDING OF THE TRAJECTORY DUE TO GRAVITY

The straight-line approximation for trajectories breaks down in the case of long (>4 s) meteors, when they will show vertical curvature that should be visible even with less precise systems. At a height of 100 km, the gravitational acceleration is $g \sim 9.5\,\mathrm{m\,s^{-2}}$, although it changes as the meteor descends through the atmosphere with the classical relation

$$g(r) = \frac{GM_\mathrm{E}}{r^2}, \tag{A1}$$

where M_E is the mass of the Earth and r is the distance of the meteor from the centre of the Earth. To compute the changing value of the gravitational acceleration, we assume that at the begin point, the downward vertical component of the meteor's velocity v_z is equal to the vertical component of the initial velocity:

$$v_z = -v_0 \cos z_\mathrm{c}, \tag{A2}$$

where v_0 is the initial velocity and z_c is the apparent zenith angle. Thus, the gravitational acceleration at a relative time t after the beginning of the meteor is

$$g(t) = \frac{GM_\mathrm{E}}{(r_0 + v_z t)^2}, \tag{A3}$$

where M_E is the mass of the Earth and r_0 is the distance from the centre of the Earth to the beginning height of the meteor. The total drop of the meteor due to gravity after time T is then

$$\Delta h(T) = \int_0^T g(t) t \, \mathrm{d}t. \tag{A4}$$

After integration, we obtain the following relation:

$$\Delta h(T) = \frac{GM_\mathrm{E}}{v_z^2} \left(\frac{r_0}{r_0 + v_z T} + \ln \frac{r_0 + v_z T}{r_0} - 1 \right). \tag{A5}$$

To avoid domain issues when $v_z \approx 0$, we only use this expanded equation if $|v_z| > 100\,\mathrm{m\,s^{-1}}$, otherwise we use equation (1) with $r = r_0$ to compute g and the classical way of computing the additional drop in height due to gravity:

$$\Delta h(T) = \frac{1}{2} g T^2. \tag{A6}$$

Applying Δh to the vertical component of the meteor at every point in time effectively simulates the curvature of the meteor's trajectory due to gravity.

APPENDIX B: DISTANCE BETWEEN LINES IN 3D SPACE

Let vector $\boldsymbol{P}$ be the position of the observer in an arbitrary rectangular coordinate system and $\boldsymbol{U}$ be the direction vector of the line of sight emanating from the observer. Let $\boldsymbol{S}$ be the position of the state vector and $\boldsymbol{R}$ be the radiant vector. The closest points of approach can be calculated as

$$\begin{aligned}
\boldsymbol{w} &= \boldsymbol{P} - \boldsymbol{S}, \\
a &= \boldsymbol{U} \cdot \boldsymbol{U}, \\
b &= \boldsymbol{U} \cdot \boldsymbol{R}, \\
c &= \boldsymbol{R} \cdot \boldsymbol{R}, \\
d &= \boldsymbol{U} \cdot \boldsymbol{w}, \\
e &= \boldsymbol{R} \cdot \boldsymbol{w}, \\
Q_\mathrm{C} &= \frac{be - cd}{ac - b^2}, \\
T_\mathrm{C} &= \frac{ae - bd}{ac - b^2}, \\
\boldsymbol{Q} &= \boldsymbol{P} + Q_\mathrm{C} \boldsymbol{U}, \\
\boldsymbol{T} &= \boldsymbol{Q} + T_\mathrm{C} \boldsymbol{R}, \\
d &= |\boldsymbol{Q} - \boldsymbol{T}|,
\end{aligned} \tag{B1}$$

where $\boldsymbol{Q}$ is the point on the observer's line of sight closest to the radiant line and $\boldsymbol{T}$ is the point on the radiant line closest to the line of sight of the observer. d is the distance between those two points. The equations are taken from Eberly (2006) in a modified form.

APPENDIX C: ORBIT COMPUTATION

The orbit is computed from four parameters: the apparent radiant unit vector $\hat{\boldsymbol{R}}$, the initial velocity v_0, the ECI coordinates of the state vector $\boldsymbol{S}$, and the reference Julian date of the beginning of the meteor $\mathrm{JD_{ref}}$. The equations below assume that the radiant and the state vector are given in the epoch of date, not J2000. Furthermore, we assume that the location of the state vector is at the beginning of the meteor, not at an average point on the trajectory. The state vector $\boldsymbol{S}$ should be in metres and the initial velocity v_0 in $\mathrm{m\,s^{-1}}$ to be consistent with constants and parameter units used herein.

First, the geocentric latitude of the state vector is calculated as

$$\varphi' = \mathrm{atan2}\left(S_z, \sqrt{S_x^2 + S_y^2}\right). \tag{C1}$$

Next, care must be taken to use the Barycentric Dynamical Time (TDB) in calculations where necessary. For epochs in 1972 and later, the dynamical time is simply calculated as the Julian date with the added leap seconds Δt up to the given JD, plus a constant of 32.184 s (Clark 2010). The number of leap seconds can be obtained from the United States Naval observatory FTP site.[1] For example, Δt for a meteor observed between 2006 and 2009 is 33 s, while for a meteor

[1]USNO leap seconds file, ftp://maia.usno.navy.mil/ser7/tai-utc.dat (accessed 2018 February 18).

observed after 2017 January 1 (until a future leap second is added) is 37 s.

$$\mathrm{TDB} = \mathrm{JD}_{\mathrm{ref}} + \frac{\Delta t + 32.184}{86\,400}. \tag{C2}$$

Next, the geodetic latitude φ and the longitude λ of the beginning point of the meteor projected on to the Earth's surface are calculated from the ECI coordinates of the state vector using the method described in Appendix D2.

C1 Correcting the apparent radiant and the velocity for Earth's rotation

If the trajectory was estimated with the IP method, or if the stations were kept fixed, one needs to correct the radiant for Earth's rotation. Please note the important fact that the correction described in this section must not be applied if the ECI coordinates of the stations were moving in time in the trajectory estimation procedure. Thus, if the station coordinates were moving during the meteor event, the velocity vector is simply calculated as

$$\boldsymbol{v}_0 = v_0 \hat{\boldsymbol{R}}, \tag{C3}$$

and the rest of the equations in this section can be skipped. Otherwise, the procedure described below must be followed.

The rotation velocity of the Earth (in $\mathrm{m\,s^{-1}}$) at the height of the state vector can be calculated as

$$v_{\mathrm{e}} = \frac{2\pi\,|\boldsymbol{S}|\cos\varphi'}{86\,164.090\,53}, \tag{C4}$$

where the number in the denominator is the duration of the sidereal day in seconds.

Next, as the direction of the Earth's rotation vector is always towards the East, we can calculate the velocity vector of the meteor $\boldsymbol{v}_0$ as

$$\begin{aligned} \boldsymbol{v}_{0x} &= v_0 \hat{R}_x - v_{\mathrm{e}} \cos\alpha_{\mathrm{e}}, \\ \boldsymbol{v}_{0y} &= v_0 \hat{R}_y - v_{\mathrm{e}} \sin\alpha_{\mathrm{e}}, \\ \boldsymbol{v}_{0z} &= v_0 \hat{R}_z, \end{aligned} \tag{C5}$$

where α_{e} is the right ascension of the direction of the rotation of the Earth. This can be calculated using the equations given in Appendix F if we take the azimuth to be $A = \pi/2$ (i.e. due East) and elevation $a = 0$.

It is very important to note that this correction only influences the direction of the radiant, but not the initial velocity itself. This is only true if ECI coordinates are used throughout, regardless of keeping the stations fixed or not.

C2 Geocentric radiant

First, we calculate equatorial coordinates of the apparent radiant following Ceplecha (1987):

$$\begin{aligned} \hat{\boldsymbol{v}}_0 &= \frac{\boldsymbol{v}_0}{|\boldsymbol{v}_0|}, \\ \alpha &= \mathrm{atan2}\left(\hat{v}_{0y}, \hat{v}_{0x}\right), \\ \delta &= \arcsin \hat{v}_{0z}. \end{aligned} \tag{C6}$$

The geocentric velocity is calculated as

$$v_{\mathrm{g}} = \sqrt{v_0^2 - \frac{2 \times 6.674\,08 \times 5.9722 \times 10^{13}}{|\boldsymbol{S}|}}, \tag{C7}$$

where the second term under the square root is the square of the escape velocity ($2GM_{\mathrm{E}}/r$) at the height of the state vector. Next, the zenith attraction correction is applied using the Schiaparelli method (Gural 2001):

$$\begin{aligned} z_{\mathrm{c}} &= \arccos\left(\sin\delta\sin\varphi' + \cos\delta\cos\varphi'\cos\left(\theta' - \alpha\right)\right), \\ \Delta z_{\mathrm{c}} &= 2\,\mathrm{atan2}\left((v_0 - v_{\mathrm{g}})\tan\frac{z_{\mathrm{c}}}{2}, v_0 + v_{\mathrm{g}}\right), \\ z_{\mathrm{g}} &= z_{\mathrm{c}} + |\Delta z_{\mathrm{c}}|, \end{aligned} \tag{C8}$$

where z_{c} is the apparent zenith angle, θ' is the apparent local sidereal time (see Appendix E), Δz_{c} is the zenith attraction correction, and z_{g} is the zenith angle of the geocentric radiant.

The azimuth A_{c} of the radiant (possibly corrected for Earth's rotation) is calculated using the equations given in Appendix G. The apparent α and δ should be used, and care must be taken to use the geocentric latitude φ' instead of the geodetic latitude. The geocentric radiant in equatorial coordinates (α_{g}, δ_{g}) is then calculated using the equations given in Appendix F, where the azimuth is $A = A_{\mathrm{c}}$, the elevation is $a = (\pi/2) - z_{\mathrm{g}}$, and the geocentric latitude φ' must be used as well.

Next, the radiant is precessed from the epoch of date ($\mathrm{JD}_{\mathrm{ref}}$) to J2000 using the equations given in Appendix H. The geocentric ecliptic longitude λ_{g} and latitude β_{g} are calculated with equations given in Appendix I; care must be taken to use the Julian date of J2000 (JD = 2 451 545) when computing ecliptic coordinates, not $\mathrm{JD}_{\mathrm{ref}}$.

C3 Precessing ECI coordinates to J2000

As the ECI coordinates of the meteor are in the epoch of date, they have to be precessed to J2000. This can easily be done by converting them to spherical coordinates:

$$\begin{aligned} r_{\mathrm{ECI}} &= |\boldsymbol{S}|, \\ \alpha_{\mathrm{ECI}} &= \mathrm{atan2}\left(S_y, S_x\right), \\ \delta_{\mathrm{ECI}} &= \arccos\frac{S_z}{r_{\mathrm{ECI}}}, \end{aligned} \tag{C9}$$

where r_{ECI} is the distance from the centre of the Earth to the reference position of the meteor, and α_{ECI} and δ_{ECI} are angular components. α_{ECI} and δ_{ECI} are precessed to J2000 from $\mathrm{JD}_{\mathrm{ref}}$ using equations given in Appendix H, after which α'_{ECI} and δ'_{ECI} are obtained. Finally, these coordinates can be converted back to rectangular ECI coordinates in J2000:

$$\begin{aligned} S'_x &= r_{\mathrm{ECI}} \sin\delta'_{\mathrm{ECI}} \cos\alpha'_{\mathrm{ECI}}, \\ S'_y &= r_{\mathrm{ECI}} \sin\delta'_{\mathrm{ECI}} \sin\alpha'_{\mathrm{ECI}}, \\ S'_z &= r_{\mathrm{ECI}} \cos\delta'_{\mathrm{ECI}}. \end{aligned} \tag{C10}$$

C4 Position and the velocity of the Earth

JPL DE430 ephemerids (Folkner et al. 2014) are used for computing Cartesian heliocentric ecliptic coordinates and the velocity of the Earth at the reference dynamical time TDB. As the implementation of the ephemerids does not allow the calculation of the heliocentric ecliptic coordinates of the Earth directly, the following procedure was adopted:

(i) The position $\boldsymbol{R}_{\rm EMB}$ and the velocity $\boldsymbol{V}_{\rm EMB}$ of the Earth–Moon barycentre with respect to the Solar system barycentre are obtained from the model in heliocentric equatorial coordinates (kilometres).

(ii) The position $\boldsymbol{R}_{\rm SB}$ and the velocity $\boldsymbol{V}_{\rm SB}$ of the centre of the Sun with respect to the Solar system barycentre are obtained from the model in heliocentric equatorial coordinates (kilometres).

(iii) The position $\boldsymbol{R}_{\rm EEM}$ and the velocity $\boldsymbol{V}_{\rm EEM}$ of the centre of the Earth with respect to the Earth–Moon barycentre are obtained from the model in heliocentric equatorial coordinates (kilometres).

The heliocentric position and the velocity of the centre of the Earth in equatorial coordinates are then computed as

$$\begin{aligned}\boldsymbol{R}_{\rm EH} &= \boldsymbol{R}_{\rm EMB} - \boldsymbol{R}_{\rm SB} + \boldsymbol{R}_{\rm EEM},\\ \boldsymbol{V}_{\rm EH} &= \boldsymbol{V}_{\rm EMB} - \boldsymbol{V}_{\rm SB} + \boldsymbol{V}_{\rm EEM},\end{aligned} \tag{C11}$$

where $\boldsymbol{R}_{\rm EH}$ and $\boldsymbol{V}_{\rm EH}$ are in km and km s^{-1}, respectively.

C5 Heliocentric coordinates of the meteor

Coordinates of the meteor in heliocentric equatorial coordinates can be calculated by simply adding the position of the Earth in heliocentric equatorial coordinates to the ECI coordinates of the meteor in J2000:

$$\boldsymbol{M} = \boldsymbol{R}_{\rm EH} + \frac{\boldsymbol{S}'}{1000}. \tag{C12}$$

Care must be taken to match the units, as the ECI coordinates were given in metres, while $\boldsymbol{M}$ should be in kilometres. Both the coordinates of the meteor $\boldsymbol{M}$ and the velocity of the Earth $\boldsymbol{V}_{\rm EH}$ have to be converted to the ecliptic reference frame by rotating them on the X-axis by the negative value of the mean obliquity of the Earth at J2000, $\epsilon_{\rm J2000} = 23.439\,291\,1111^\circ$:

$$\begin{bmatrix} x_{\rm ecliptic} \\ y_{\rm ecliptic} \\ z_{\rm ecliptic} \end{bmatrix} = \begin{bmatrix} 1 & 0 & 0 \\ 0 & \cos(-\epsilon_{\rm J2000}) & \sin(-\epsilon_{\rm J2000}) \\ 0 & -\sin(-\epsilon_{\rm J2000}) & \cos(-\epsilon_{\rm J2000}) \end{bmatrix} \begin{bmatrix} x_{\rm equatorial} \\ y_{\rm equatorial} \\ z_{\rm equatorial} \end{bmatrix}, \tag{C13}$$

after which $\boldsymbol{M}'$ and $\boldsymbol{V}'_{\rm EH}$ in heliocentric ecliptic coordinates are obtained.

The heliocentric velocity vector of the meteor is calculated by adding the geocentric velocity of the meteor to the velocity of the Earth. As $\boldsymbol{V}'_{\rm EH}$ is in heliocentric ecliptic coordinates, we convert the geocentric velocity into an ecliptic velocity vector ($\lambda_{\rm g}$ and $\beta_{\rm g}$ can be computed using equations in Appendix I):

$$\begin{aligned} v_{{\rm gE}x} &= -v_{\rm g}\cos\lambda_{\rm g}\cos\beta_{\rm g},\\ v_{{\rm gE}y} &= -v_{\rm g}\sin\lambda_{\rm g}\cos\beta_{\rm g},\\ v_{{\rm gE}z} &= -v_{\rm g}\sin\beta_{\rm g}\end{aligned} \tag{C14}$$

and add it to the velocity of the Earth around the Sun to obtain the heliocentric velocity vector $\boldsymbol{v}_{\rm H}$:

$$\boldsymbol{v}_{\rm H} = \boldsymbol{V}'_{\rm EH} + \frac{\boldsymbol{v}_{\rm gE}}{1000}, \tag{C15}$$

where $\boldsymbol{v}_{\rm H}$ and $\boldsymbol{V}'_{\rm EH}$ are in km s^{-1}, and $\boldsymbol{v}_{\rm gE}$ is in m s^{-1}.

C6 Heliocentric ecliptic radiants

Tsuchiya et al. (2017) have shown that low-velocity meteor showers suffer from large dispersion in geocentric equatorial coordinates due to the component of Earth's velocity. They propose calculating radiants in heliocentric ecliptic coordinates, as slower meteor showers show significantly lower dispersions in that coordinate system. For completeness, we give the equations below.

The unit heliocentric velocity vector of the meteoroid is calculated as

$$\hat{\boldsymbol{V}}_{\rm c} = \frac{\boldsymbol{v}_{\rm H}}{|\boldsymbol{v}_{\rm H}|} \tag{C16}$$

and the radiant in heliocentric ecliptic coordinates is then calculated as

$$\begin{aligned}\lambda_{\rm h} &= {\rm atan2}\left(\hat{V}_{{\rm c}y}, \hat{V}_{{\rm c}x}\right) + \pi,\\ \beta_{\rm h} &= -\arcsin\hat{V}_{{\rm c}z}.\end{aligned} \tag{C17}$$

C7 Keplerian orbital elements

The solar longitude $\lambda_\odot$ can be calculated from the ecliptic heliocentric position of the Earth $\boldsymbol{R}'_{\rm EH}$, which can be computed by rotating the equatorial heliocentric position $\boldsymbol{R}_{\rm EH}$ using equation (13).

$$\lambda_\odot = {\rm atan2}\left(R'_{{\rm EH}y}, R'_{{\rm EH}x}\right) + \pi. \tag{C18}$$

The specific orbital energy ϵ can be calculated as

$$\epsilon = \frac{|\boldsymbol{v}_{\rm H}|^2}{2} - \frac{\mu_\odot}{|\boldsymbol{M}'|}, \tag{C19}$$

where $\boldsymbol{v}_{\rm H}$ is the heliocentric ecliptic velocity vector of the meteor, $\mu_\odot = 1.327\,124\,400\,18 \times 10^{11}$ km^3 s^{-2} is the gravitational constant of the Sun, and $\boldsymbol{M}'$ is the heliocentric ecliptic position vector of the meteoroid.

The semimajor axis in au is

$$a = \frac{-\mu_\odot}{2\epsilon r_{\rm au}}, \tag{C20}$$

where $r_{\rm au} = 149\,597\,870.7$ km is one astronomical unit in kilometres. Mean motion in radians per day can be calculated as

$$n = 86\,400\sqrt{\frac{G{\rm M}_\odot}{(1000|a|r_{\rm au})^3}}, \tag{C21}$$

where $G = 6.673\,84 \times 10^{-11}$ m^3 kg^{-1} s^{-2} is the gravitational constant and ${\rm M}_\odot = 1.988\,55 \times 10^{30}$ kg is the mass of the Sun. The orbital period in years is

$$T = \frac{2\pi}{86\,400 Y_{\rm S}}\sqrt{\frac{(r_{\rm au}a)^3}{\mu_\odot}}, \tag{C22}$$

where $Y_{\rm S} = 365.256\,363\,004$ is the sidereal year in days. Next, we calculate the orbital angular momentum vector

$$\boldsymbol{h} = \boldsymbol{M}' \times \boldsymbol{v}_{\rm H}. \tag{C23}$$

The inclination is then simply

$$i = \arccos\frac{h_z}{|\boldsymbol{h}|} \tag{C24}$$

and the eccentricity is then the magnitude of the eccentricity vector:

$$\begin{aligned}\boldsymbol{e} &= \frac{\boldsymbol{v}_{\rm H}\times\boldsymbol{h}}{\mu_\odot} - \frac{\boldsymbol{M}'}{|\boldsymbol{M}'|},\\ e &= |\boldsymbol{e}|\,.\end{aligned} \tag{C25}$$

We follow Jenniskens et al. (2011) on calculating the perihelion distance:

$$q = \begin{cases} \frac{|\boldsymbol{M}'|+\boldsymbol{e}\cdot\boldsymbol{M}'}{2}, & e = 1,\\ a(1-e), & \text{otherwise.}\end{cases} \tag{C26}$$

The aphelion distance is then simply

$$Q = a(1 + e). \tag{C27}$$

The ascending node Ω is calculated following Clark (2010):

$$\boldsymbol{k} = [0, 0, 1],$$

$$\boldsymbol{n} = \boldsymbol{k} \times \boldsymbol{h}, \tag{C28}$$

$$\Omega = \begin{cases} 0, & |\boldsymbol{n}| = 0, \\ \text{atan2}\left(n_y, n_x\right), & \text{otherwise}, \end{cases} \tag{C29}$$

where $\boldsymbol{n}$ is a vector pointing from the Sun to the ascending node. Please note that the ascending node loses meaning for inclinations close to 0°; thus, we keep the node at 0° when the magnitude of the $\boldsymbol{n}$ vector is 0.

If $|\boldsymbol{n}| \neq 0$, the argument of perihelion ω is calculated as

$$\omega = \arccos \frac{\boldsymbol{n} \cdot \boldsymbol{e}}{|\boldsymbol{n}||\boldsymbol{e}|}, \tag{C30}$$

and if $e_z < 0$, then $\omega = 2\pi - \omega$. If, on the other hand, $|\boldsymbol{n}| = 0$, then

$$\omega = \arccos \frac{e_x}{|\boldsymbol{e}|}. \tag{C31}$$

The longitude of perihelion ϖ is simply

$$\varpi = \Omega + \omega. \tag{C32}$$

True anomaly ν is calculated as

$$\nu = \arccos \frac{\boldsymbol{e} \cdot \boldsymbol{M}'}{|\boldsymbol{e}||\boldsymbol{M}'|}, \tag{C33}$$

and if $\boldsymbol{M}' \cdot \boldsymbol{v}_{\rm H} < 0$, then $\nu = 2\pi - \nu$.

The eccentric anomaly E is

$$E = \text{atan2}\left(\sqrt{1 - e^2}\sin\nu, e + \cos\nu\right), \tag{C34}$$

from which the mean anomaly M can be calculated as

$$M = E - e\sin E. \tag{C35}$$

The time in days since the last perihelion passage, reference to TDB, is

$$\Delta t_{\varpi} = \frac{Ma^{3/2}}{k}, \tag{C36}$$

where $k = 0.017\,202\,098\,95\,\text{au}^{3/2}\,\text{d}^{-1}\,(\text{solar mass})^{-1/2}$ is the Gaussian gravitational constant.

Finally, we calculate the Tisserand parameter with respect to Jupiter as

$$T_{\rm J} = \frac{a_{\rm J}}{a} + 2\sqrt{(1 - e^2)\frac{a}{a_{\rm J}}}\cos i, \tag{C37}$$

where $a_{\rm J} = 5.204\,267$ au is the semimajor axis of Jupiter.

APPENDIX D: EARTH-CENTRED INERTIAL COORDINATES

The ECI coordinates are a Cartesian coordinate system where the *X*–*Y* plane coincides with the equatorial plane of the Earth, and the *X*-axis passes through the equinox of the given epoch. The *Z*-axis passes through the Earth's North pole. As the coordinate system is permanently fixed to the celestial sphere, a fixed point on the surface of the Earth will have changing coordinates in time. As we assume that the observations are given in the epoch of date, we keep the ECI coordinates in the epoch of date as well.

Let the distance from the centre of the Earth to the position given by geographical coordinates in the WGS84 system be calculated as follows:

$$N = \frac{r_{\rm e}}{\sqrt{1 - e_{\rm e}^2\sin^2\varphi}}, \tag{D1}$$

where $r_{\rm e}$ is the equatorial radius of the Earth as defined by the WGS84 system, $r_{\rm e} = 6\,378\,137.0$ m, and $e_{\rm e}$ is the equatorial ellipticity of an oblate Earth:

$$e_{\rm e} = \sqrt{1 - \frac{r_{\rm e}^2}{r_{\rm p}^2}}, \tag{D2}$$

where $r_{\rm p}$ is the polar radius of the Earth, $r_{\rm p} = 6\,356\,752.314\,245$ m. The polar ellipticity is

$$e_{\rm p} = \sqrt{1 - \frac{r_{\rm e}^2 - r_{\rm p}^2}{r_{\rm p}^2}}. \tag{D3}$$

D1 Converting geographical coordinates to ECI

Let φ be the geodetic latitude, λ the longitude, h the height above a WGS84 model for Earth, and θ' ar radius of the Earth, eqn_1c885-10237 . The polar ellipticity is D1 Converting geographical coordinates to ECI Let φ be the geodetic latitude, λ the longitude, h the height above a WGS84 model for Earth, and eqn_149a9-1ffbe 2012he apparent local s θ' can be calculated using the procedure described on p. 88 of Meeus (1998) and Clark (2010); see Appendix E for equations.

First, the coordinates are transformed into ECEF coordinates:

$$\begin{aligned} x_{\rm ECEF} &= (N + h)\cos\varphi\cos\lambda, \\ y_{\rm ECEF} &= (N + h)\cos\varphi\sin\lambda, \\ z_{\rm ECEF} &= \left((1 - e_{\rm e}^2)N + h\right)\sin\varphi. \end{aligned} \tag{D4}$$

The radius of the Earth at the given geodetic latitude is then

$$R_{\rm h} = \sqrt{x_{\rm ECEF}^2 + y_{\rm ECEF}^2 + z_{\rm ECEF}^2}. \tag{D5}$$

Using the geocentric latitude φ',

$$\varphi' = \text{atan2}\left(z_{\rm ECEF}, \sqrt{x_{\rm ECEF}^2 + y_{\rm ECEF}^2}\right). \tag{D6}$$

The ECI coordinates in the epoch of date are then calculated as

$$\begin{aligned} x_{\rm ECI} &= R_{\rm h}\cos\varphi'\cos\theta', \\ y_{\rm ECI} &= R_{\rm h}\cos\varphi'\sin\theta', \\ z_{\rm ECI} &= R_{\rm h}\sin\varphi'. \end{aligned} \tag{D7}$$

D2 ECI to geographical coordinates

Given the apparent sidereal time at Greenwich θ_0' (see equation and Clark (2010); see Appendix E for equations. Fi), the longitude can be calculated as

$$\lambda = \text{atan2}\left(y_{\rm ECI}, x_{\rm ECI}\right) - \theta_0'. \tag{D8}$$

d into ECEF coordinates: The radius of the Earth at the given geodetic latitude is then Usin

$$p = \sqrt{x_{\rm ECI}^2 + y_{\rm ECI}^2},$$

$$\vartheta = \text{atan2}\left(z_{\rm ECI} r_{\rm e},\, p r_{\rm p}\right),$$

$$\varphi = \text{atan2}\left(z_{\rm ECI} + e_{\rm p}^2 r_{\rm p} \sin^3\vartheta,\, p - e_{\rm e}^2 r_{\rm e} \cos^3\vartheta\right). \quad \text{(D9)}$$

Care must be taken when calculating the height near exact poles due to numerical instabilities. If the coordinates are near the poles, and we take this as being within 1 km from the poles, which can be determined by testing whether both conditions $|x_{\rm ECI}| < 1000$ and $|y_{\rm ECI}| < 1000$ are true, the height is calculated as

$$h = |z_{\rm ECI}| - r_{\rm p}, \quad \text{(D10)}$$

otherwise the height above a WGS84 ellipsoid is calculated as

$$N = \frac{r_{\rm e}}{\sqrt{1 - e_{\rm e}^2 \sin^2\varphi}},$$

$$h = \frac{p}{\cos\varphi} - N. \quad \text{(D11)}$$

ting the height near exact poles due to numerical instabilities. If the coordinates are near the poles, and we take this as being within 1 km from the poles, which can be determined by testing whether both conditions | x ECI | < 1000 and | y ECI | < 1000 are true, th2012) has to be applied.

APPENDIX E: LOCAL APPARENT SIDEREAL TIME

First, we calculate the nutation components $\Delta\psi$ and $\Delta\epsilon$ in equation (f the height above meansea level (MSL)) as given in chapter 22 of Meeus (1998). We use the set of equations that give around 0.5 arcsec precision, which we deem sufficient for needs of meteoroid orbits. The dynamical time TDB is used. Ω is the longitude of the ascending node of the Moon's mean orbit on the ecliptic measured from the mean equinox of the date, L is the mean longitude of the Sun, and L' is the mean longitude of the Moon. The values are in degrees.

$$T = \frac{\text{TDB} - 2\,451\,545}{36\,525},$$

$$\Omega = 125.044\,52 - 1934.136\,261 T,$$

$$L = 280.4665 + 36\,000.7698 T,$$

$$L' = 218.3165 + 48\,1267.8813 T. \quad \text{(E1)}$$

The nutation in longitude $\Delta\psi$ and the nutation in obliquity $\Delta\epsilon$ are calculated in arcseconds as

$$\Delta\psi = -17.2\sin\Omega - 1.32\sin 2L - 0.23\sin 2L' + 0.21\sin 2\Omega,$$

$$\Delta\epsilon = 9.2\cos\Omega + 0.57\cos 2L + 0.1\cos 2L' - 0.09\cos 2\Omega. \quad \text{(E2)}$$

Next, we calculate the mean sidereal time of the Earth (Greenwich Sidereal Time) in degrees. Note that the time used here is not dynamical.

$$t = \frac{\text{JD} - 2\,451\,545}{36\,525},$$

$$\theta_0 = 280.460\,618\,37 + 360.985\,647\,366\,29(\text{JD} - 2\,451\,545) + 0.000\,387\,933 t^2 - \frac{t^3}{38\,710\,000}. \quad \text{(E3)}$$

The mean obliquity of the Earth in arcseconds ϵ_0 is calculated using U, which is the time measured in units of 10 000 Julian years from J2000 (note that the dynamical time is used):

$$U = \frac{\text{TDB} - 2\,451\,545}{3\,652\,500},$$

$$\epsilon_0 = 84\,381.448 - 4680.93U - 1.55U^2 + 1999.25U^3 - 51.38U^4 - 249.67U^5 - 39.05U^6 + 7.12U^7 + 27.87U^8 + 5.79U^9 + 2.45U^{10}. \quad \text{(E4)}$$

Sidereal Time) in degrees. Note that the time used here is not dynamical. The mean obliquity o

$$\theta_0' = \theta_0 + \frac{\Delta\psi}{3600}\cos\frac{\epsilon_0 + \Delta\epsilon}{3600}. \quad \text{(E5)}$$

f the Earth in arcseconds ϵ 0 is calculated using U , which is the time measured in units of 10 000 Julian years from J2000 (note that the dynam 2π] range using modulus operator:

$$\theta_0' = \theta_0' \bmod 2\pi. \quad \text{(E6)}$$

parent sidereal time at Greenwich θ' etion> converting to

$$\theta' = (\theta_0' + \lambda + 2\pi) \bmod 2\pi, \quad \text{(E7)}$$

> radians, care must be taken to wrap the computed value inside the [0, eqn_16e86-1928d] range using

APPENDIX F: HORIZONTAL TO EQUATORIAL COORDINATE CONVERSION

Right ascension α and declination δ are calculated from azimuth A, altitude a, Julian date JD, and geographical coordinates of the observer, longitude λ and latitude φ, as

$$H = \text{atan2}\left(-\sin A,\, \tan a\cos\varphi - \cos A\sin\varphi\right),$$

$$\alpha = \theta' - H,$$

$$\delta = \arcsin\left(\sin\varphi\sin a + \cos\varphi\cos a\cos A\right), \quad \text{(F1)}$$

where H is the local hour angle and θ' is the apparent local sidereal time (see Appendix E).

APPENDIX G: EQUATORIAL TO HORIZONTAL COORDINATE CONVERSION

The azimuth A and altitude a are calculated from right ascension α, declination δ, Julian date JD, and geographical coordinates of the observer, longitude λ and latitude φ, as

$$\begin{aligned} H &= \theta' - \alpha, \\ A &= \pi + \operatorname{atan2}(\sin H, \cos H \sin\varphi - \tan\delta \cos\varphi), \\ a &= \arcsin(\sin\varphi \sin\delta + \cos\varphi \cos\delta \cos H), \end{aligned} \tag{G1}$$

where H is the local hour angle and θ' is the apparent local sidereal time (see Appendix E).

APPENDIX H: PRECESSING EQUATORIAL COORDINATES

We follow the rigorous method of Meeus (1998), pp. 134–135, for precessing the right ascension α and declination δ from epoch JD_0 to epoch JD. The beginning of each epoch is defined by their respective Julian dates. Please note that ζ, z, and θ are given in degrees.

$$\begin{aligned} T &= \frac{\mathrm{JD}_0 - 2\,451\,545}{36\,525}, \\ t &= \frac{\mathrm{JD} - \mathrm{JD}_0}{36\,525}, \\ \zeta &= \frac{1}{3600}\left[(2306.2181 + 1.396\,56T - 0.000\,139T^2)t \right. \\ &\quad \left. + (0.301\,88 - 0.000\,344T)t^2 + 0.017\,998t^3\right], \\ z &= \frac{1}{3600}\left[(2306.2181 + 1.396\,56T - 0.000\,139T^2)t \right. \\ &\quad \left. + (1.094\,68 + 0.000\,066T)t^2 + 0.018\,203t^3\right], \\ \theta &= \frac{1}{3600}\left[(2004.3109 - 0.853\,30T - 0.000\,217T^2)t \right. \\ &\quad \left. - (0.426\,65 + 0.000\,217T)t^2 - 0.041\,833t^3\right], \\ A &= \cos\delta \sin(\alpha + \zeta), \\ B &= \cos\theta \cos\delta \cos(\alpha + \zeta) - \sin\theta \sin\delta, \\ C &= \sin\theta \cos\delta \cos(\alpha + \zeta) + \cos\theta \sin\delta, \\ \alpha' &= \operatorname{atan2}(A, B) + z, \\ \delta' &= \arcsin C, \end{aligned} \tag{H1}$$

where α' and δ' are precessed coordinates. If the declination is close to the celestial poles (which we define as less than 0.5° from the poles), it is calculated differently due to numerical instabilities. If $(90^\circ - |\delta|) < 0.5^\circ$ is true, the declination should be calculated as

$$\delta' = \arccos\sqrt{A^2 + B^2}. \tag{H2}$$

APPENDIX I: ECLIPTIC COORDINATES

The geocentric right ascension α_g and declination δ_g at the given epoch (the epoch defined by a Julian date JD, usually at J2000; thus, JD = 2 451 545) can be converted to geocentric ecliptic longitude λ_g and latitude β_g with the procedure described below. First, a precise obliquity of the Earth at the JD of the epoch has to be calculated; $\Delta\epsilon$ can be calculated using equation (l instabilities. If $(90^\circ -$) and the mean obliquity ϵ_0 using equation (ld be calculated as APPENDIX I: ECLIPTIC COORDINATES The geocentric right ascension α g and declinat). The true obliquity of the Earth in degrees is then simply

$$\epsilon = \frac{\epsilon_0 + \Delta\epsilon}{3600}. \tag{I1}$$

The ecliptic longitude and latitude are then

$$\begin{aligned} \lambda_g &= \operatorname{atan2}\left(\sin\epsilon \sin\delta_g + \sin\alpha_g \cos\delta_g \cos\epsilon, \cos\alpha_g \cos\delta_g\right), \\ \beta_g &= \arcsin\left(\cos\epsilon \sin\delta_g - \sin\alpha_g \cos\delta_g \sin\epsilon\right). \end{aligned} \tag{I2}$$

This paper has been typeset from a TEX/LATEX file prepared by the author.